Politecnico di Torino

Corso di Laurea Magistrale in Ingegneria Aerospaziale

Master's Thesis

Aeroacoustic-source analysis of a structured porous coated cylinder

Supervisors:

Prof. Francesco Avallone

Prof. Riccardo Zamponi

Dr. Alessandro Zarri

Candidate:

Francesco Burruni

Academic year 2024/2025

Abstract

The aerodynamic noise generated by a circular cylinder in uniform flow represents a central topic in many engineering and environmental applications, such as high-speed train pantographs, landing gear systems, etc. In recent years, it has been proven that coating a circular cylinder with a porous medium represents an effective noise mitigation. However, the precise mechanism through which this suppression performance is achieved is not clear yet. In the most common view according to the Curle's analogy, the aerodynamic noise generated by a cylinder in uniform flow can be modelled, in equivalent terms, by a surface distribution of dipolar sources associated with pressure fluctuations acting on the cylinder surface and by volumetric sources located in the wake, linked to the unsteady velocity fluctuations. At low Mach numbers, the latter contribution is typically overshadowed by the dipolar one. However, recent studies have shown that this assumption does not necessarily hold for a porous-coated cylinder. Indeed, by means of source-localization techniques, it has been found that the dominant acoustic sources lie in the wake rather than on the cylinder surface. As a result, the acoustic field emitted by a porous cylinder can be formulated as a problem of diffraction of flow sources (i.e., quadrupole) by the rigid body. The present work aims to provide a physical explanation for this phenomenon and clarify the link between flow-field alterations and related noise mitigation performance of a porous-coated circular cylinder. For this purpose, a structured porous medium, which means that pores are spread with regularity around the bare cylinder, and an existing data set coming from a high-fidelity simulation based on the Lattice Boltzmann method have been employed. Results of this simulation are post-processed to compute far-field data employing the Ffowcs Williams and Hawkings (FWH) formulation that predicts aerodynamic noise from unsteady flow data around moving bodies. In the low frequency regime, analysis of far-field data reveals that aerodynamic noise is dominated by quadrupolar sources located in the wake, contradicting the general view that considers the quadrupolar contribution negligible at low Mach numbers. The relevance of the quadrupolar sources is also confirmed through a coherence analysis between velocity fluctuations, near-field pressure, and far-field pressure, revealing that the former have a more pronounced effect on the far-field. The analysis of the flow field demonstrates that a downstream shift of the onset of vortex shedding occurs, increasing what is normally referred to as the "vortex formation length".

This effect has a relevant impact on the aeroacoustic results, since, according to the diffraction theory, it leads to a loss of efficiency of the scattering mechanism, which results in the dipolar source having a minor impact on the far-field noise. The existence of such a feedback mechanism is supported by the results of the spectral proper orthogonal decomposition (SPOD), which suggests that turbulent velocity fluctuations are responsible for imposing surface pressure fluctuations on the surface at the vortex shedding frequency. This hypothesis is also confirmed by a coherence analysis between near-field pressure and velocity fluctuations. The outcome of this thesis is expected to provide guidelines for a more effective design of noise-mitigation strategies applied to circular cylinders.

Contents

Thesis's outline

The main topic of the present work is to understand the role of the quadrupolar source in the case of flow cylinder noise. An existing data-set of an high fidelity simulation will be post-processed to compute far-field data with both permeable and solid FWH formulation to assess the contribution of quadrupolar and dipolar sources. A physical interpretation of these aeroacoustic results will be provided exploring a connection between wake development and aerodynamic noise attenuation. Then a physical interpretation of what, in equivalent terms, we normally call scattering mechanism will be provided. The mechanism through which near-field pressure fluctuations are imposed will be analysed through a coherence analysis and in this regard the existence of a feedback contribution which originates in the wake, propagates upstream and induces surface pressure fluctuations at the shedding frequency is investigated post-processing SPOD results performed in the wake of porous cylinder. The thesis will be organized as follows: in the first section a brief literature review is provided focusing on the role of quadrupole, the mechanism of noise reduction and the benefits of porous configuration. The second chapter is reserved to the theoretical background, where the diffraction theory will be enunciated, while in the third chapter the set-up of the simulation is described. In the fourth chapter aeroacoustic results will be presented and analysed and a physical interpretation of them will be provided in the following chapter. In the sixth chapter a coherence analysis between near-field pressure and velocity fluctuations will be performed, while in the following chapter SPOD results are post-processed focusing on the investigation of the feedback contribution. In the final chapter, conclusions about results found in the previous chapters will be drawn. Guidelines for a more effective noise mitigation performance for circular cylinders will be provided and finally some further investigations for possible future works will be proposed.

Chapter 1: Introduction

The study of aerodynamic noise generated by a cylinder in crossflow has numerous applications in engineering and industrial fields. A notable example is the case of high-speed trains, where aerodynamic noise becomes particularly intense when the train reaches speeds above 300 km/h. Reducing and, more generally, controlling this noise could significantly enhance the comfort of both passengers and nearby residents. A similar situation is found in the aeronautical field, where the landing gear system represents one of the primary sources of aerodynamic noise. Reducing this noise could lead to significant environmental benefits, particularly around airports, where the landing gear is typically deployed. There are numerous other scenarios where mitigating noise generated by a cylinder, or bodies resembling its shape, would be advantageous. When a cylinder is placed in crossflow, a two-dimensional model exhibits a periodic shedding of vortices from the upper and lower surfaces, leading to the formation of the well-known Von Kármán vortex street. This phenomenon is characterized by a shedding frequency (f_{SH}), which generates a strong tonal noise component commonly referred to as the "Aeolian tone." In a three-dimensional model, however, the flow in the near wake becomes more complex. For finite wall-mounted cylinders, the mean flow is characterized by four distinct vortex systems: tip vortices, base vortices, Von Kármán vortices (similar to those in the two-dimensional model), and a horseshoe vortex, which has the least influence. Furthermore, additional geometric parameters, such as the aspect ratio (length-to-diameter ratio), affect the flow dynamics. When the aspect ratio falls below a critical value, vortex shedding ceases. The boundary layer height relative to the cylinder length also influences the strength of the base vortices. All these parameters alter the flow-induced noise, affecting both the strength and frequency of the Aeolian tone. Specifically, the frequency of the Aeolian tone is generally lower than that measured in the two-dimensional model, while the intensity of the noise increases with higher aspect ratios, as the influence of tip vortices diminishes and the mid-vortices (i.e., the Von Kármán street) can organize themselves similarly to the two-dimensional configuration. Although the impact of the boundary layer height in the incoming flow has not yet been fully clarified, many experimental studies have shown that increasing boundary layer height affects the development of tip and base vortices, leading to the formation of a Von Kármán vortex street even at low aspect ratios.

To improve aeroacoustics performance, various flow control techniques can be employed to eliminate or delay flow separation, inhibit vortex shedding noise, and, consequently, reduce aerodynamic noise. These techniques can be categorized into active and passive methods. Typical examples of active methods include fluid suction or blowing and the use of plasma actuators. Among passive methods, one that has gained significant attention in recent years is the application of porous coatings on the surface of circular cylinders. These coatings help control aerodynamic noise at the source, distinguishing them from insulation methods, which aim to block sound propagation. Several experimental and numerical studies have been conducted to explore the effectiveness of porous materials in mitigating noise from cylinders.

1.1 Literature review

The noise generated by the flow past a non-vibrating cylinder is linked to the interaction between unsteady vortices, which periodically detach from upper and lower surface forming the Von Karman street. In the most common view the noise is generated by this street of vortices, which induce a reaction force exerted by surface on the surrounding fluid. Following the Curle's analogy, this fluctuating force is linked to the pressure fluctuations acting on the surface and the resulting acoustic field can be modelled with a distribution of surface dipoles. At low Mach numbers and under the assumption of acoustically compactness, which means that variations of retarded time can be neglected, this surface term dominates over the volume term, that has a quadrupolar-like field and accounts for the noise generated by instability inside the flow, so it has to be intended as an equivalent source to the phenomena that occur in the source region. However it is important to stress that acoustic energy cannot come from the aforementioned fluctuating reaction force, since it is exerted on a rigid surface. As a consequence the source of acoustic energy must be located in the flow itself and the dipole-like field must be considered the result of scattering of the quadrupolar sources by the body. This reasoning seems to be contradictory respect to the hypothesis proposed by Curle's analogy, however X. Gloerfelt et al. demonstrate by means of a tailored Green's function that for a cross-flow cylinder the whole acoustic field is dominated by dipole-like field. Focusing on the

latter, its strength per unit volume is proportional to the Lighthill's tensor T_{ij} defined in the following way:

$$T_{ij} = \rho u_i u_j + p\delta_{ij} - c_\infty^2 \rho \delta_{ij} + \tau_{ij}$$

(1. 1)

Where u_i, u_j are velocity components and ρ, p, δ_{ij} and τ_{ij} are density, pressure, Kronacker's delta and viscous stress tensor respectively. It accounts not only for the generation of sound, but also for its convective transportation and its dissipation by means of conduction and viscosity. Neglecting the stress tensor and hypothesizing an isentropic propagation Lighthill's tensor becomes $T_{ij} \cong \rho_0 u_i u_j$ and, according to the Lighthill's analogy, it can be seen as the tensor of momentum flux across a fixed surface in a fluctuating flow, or alternatively as the "fluctuating Reynolds stresses", and it has the most striking impact in the noise generation. Its strength is largely determined by large structures, where the greatest part of turbulent kinetic energy is concentrated, while the small structures have a negligible contribution. Moreover using the total enthalpy as acoustic variable, when the vorticity is localised in the space and the entropy gradients are non-zero, this source term can be replaced by:

$$T_{ij} = \rho_0(\boldsymbol{\omega} \wedge \boldsymbol{v})$$

(1. 2)

Where $\boldsymbol{\omega}$ is the vorticity vector and the viscous dissipation of the kinetic energy is neglected. As it can be easily noted, quadrupole strength is proportional to the square of a flow characteristic velocity, as a result the radiated field and the correspondent intensity depend on the fourth and eighth power of the same velocity respectively. Regarding the location of the quadrupole in the problem of flow induced noise past a cylinder, it will be localised in the wake downstream the cylinder, precisely at a distance where the counter-rotating vortices shed by the cylinder surface start to interact, as their the interaction is the primary noise source. As a consequence of what is stated above, a reduction on the unsteadiness in the wake leads to an improvement in the acoustic performance. In the following part of this section, many studies about the effects of porous coating on the noise suppression are briefly analysed.

One of the earliest studies in this area was conducted by Sueki et al., who performed wind tunnel experiments to compare the aerodynamic and aeroacoustics performance of bare and coated cylinders, highlighting the advantages of the latter. Their research focused on the correlation between aeroacoustics fields, fluctuations in aerodynamic forces, and the pressure distribution around the cylinder in both cases. In terms of aerodynamic noise, they found that the bare cylinder produced intense narrow-band noise with a peak near the vortex shedding frequency. In contrast, the coated cylinders exhibited no such narrow-band peak and had significantly lower sound pressure levels, confirming the effectiveness of the porous coating in reducing aerodynamic noise. The study also examined lift force fluctuations and the coherence between aerodynamic noise and lift force. It was found that lift fluctuations were reduced for the coated cylinders compared to the bare one, and the coherence between aerodynamic noise and lift force was lower for the coated configurations (the bare cylinder exhibited a strong coherence peak near the shedding frequency). These results suggest that reducing lift fluctuations contributes to the attenuation of aerodynamic noise. Additionally, pressure coefficient distributions and velocity profiles in the wake were measured to investigate the flow dynamics around the cylinders. The pressure coefficient revealed that the flow around the coated cylinder accelerates more slowly compared to the bare cylinder, indicating that the porous coating dissipates momentum from the flow. In contrast, the coated cylinder had a region where velocity fluctuations were significantly suppressed, and this region was shifted downstream and widened in the y-direction. The vorticity contours also demonstrated a suppression of time variations in vorticity, which is directly related to the reduction of aerodynamic noise, as the interaction of unstable vortices is a primary noise source. Another significant study in this field was conducted by Geyer, who carefully varied key material parameters, such as porosity, airflow resistivity, and coating thickness, to analyse their effect on tonal peaks and broadband noise. Airflow resistivity, in particular, was found to have a substantial impact on both tonal and broadband noise. Materials with low airflow resistivity were more effective in reducing broadband noise, particularly at low Reynolds numbers. For tonal noise, the use of porous materials led to a narrowing of the vortex shedding peak and slight variations in shedding frequency across different materials.

An increase in coating thickness further reduced broadband noise and narrowed the tonal peak, with these effects being more pronounced in materials with low airflow resistivity. However, the peak values of sound pressure levels for the coated cylinders could be either higher or lower than those of the bare cylinder, depending on various factors such as geometry (e.g., thickness-to-diameter ratio), material properties (high porosity and low airflow resistivity were beneficial), and Reynolds number (noise reduction became more effective at higher Reynolds numbers). However, these trends may not hold when different parameters from those used in the study are considered. Finally, to conclude the study the turbulence spectral density and spanwise coherence are analysed. Regarding the spectrum of turbulence velocity fluctuations, since a similar trend to that of the SPL is found, the effect of the porous is the same on the velocity fluctuations and on the acoustic pressure radiated as noise. The spanwise coherence measured for non-porous cylinder shows an extent much smaller than that of the porous one. So, the presence of the coating leads to higher peak level of the velocity fluctuations in the wake and to a greater extension where the turbulence structures are still correlated. Moreover this means that the mechanism of noise reduction is not linked to a disturbance of a spanwise coherence. Comparable results were found by Geyer et Sarradj, who carried out acoustic measurements in a small acoustic wind tunnel on a set of circular cylinders divided into three categories according to their value of air-flow resistivity (low, medium and high air-flow resistivity) and they studied their effect on noise suppression. Regardless the air-flow resistivity, the porous cover does not lead to a complete suppression of the tonal peak, in accordance with the findings of Geyer. However this result does not agree with Sueky at al., who found a complete suppression of the tonal, this difference is probably due to the use of materials with relatively high value of air-flow resistivity in the present study. However, it is important to note that, although the tonal peaks observed in porous configurations are generally narrower than those in the baseline configuration, a reduction of 10-15 dB in the tonal peak's integral is achieved. As for broadband noise, materials with lower air-flow resistivity demonstrate superior noise reduction performance compared to those with medium to high resistivity. At high Reynolds numbers and elevated frequencies, a notable noise reduction is observed, although the reduction remains modest, typically below 5 dB.

Sharma et al. conducted both numerical and experimental investigations on porous-coated cylinders, focusing on varying the ratio of porous coating thickness to the cylinder's diameter, as well as the airflow resistivity, in order to achieve optimal noise attenuation. The study confirmed trends observed in previous research, showing that adding a porous coating to a cylinder affected flow dynamics significantly. The porous coating relaxed the shear layer, synchronizing vortex shedding, and expanded the low-speed wake region compared to the bare cylinder. Materials with low airflow resistivity resulted in weaker flow modifications, with higher-energy structures being expelled into the wake, while high resistivity materials reduced flow entrainment and produced more complex vortical structures. Moreover the analysis revealed that porous coatings reduce the amplitude of lift and drag coefficients, with higher permeability materials showing the greatest reductions. To conclude the analyse, the far field sound pressure level versus Strouhal number is recorded for all porous coated cylinders at fixed Reynolds number. Porous coatings with medium-low airflow resistivity reduce both the peak value and peak frequency of the tonal noise respect to the bare case. But this positive effect fails if the coating with the lowest permeability is considered, this implies that an high flow entrainment within the pores is required to achieve an acceptable noise reduction. A Similar work is performed by H. Liu et al., where LES equations for two-dimensional incompressible flow are resolved numerically and the results of the simulation are used as input to predict the far-field aerodynamic noise through the FWH (Ffowcs Williams Hawkings) equation. The study investigates the effects of porosity, pore density (PPI), and coating thickness on noise reduction, with SPL plotted against frequency. Higher porosity significantly lowers the dominant tonal peak, shifts it to lower frequencies, and reduces overall noise across the spectrum below 1000 Hz. Increased PPI and thickness show similar benefits, though porosity is the most impactful parameter. Additionally, porous coatings effectively reduce drag and lift amplitude and influence their frequency, particularly at higher porosity levels, by altering vortex shedding dynamics. Aguiar et al. conducted an experimental study to investigate the effects of a porous coating on both the pressure distribution around a cylinder and the wake pattern. The pressure distribution was analysed using pressure taps, while the wake pattern was studied through Laser Doppler Anemometry (LDA). Additionally, they examined the coating's impact on noise suppression.

The porous coating enhances the overall pressure coefficient on the cylinder, redistributing pressure and reducing the pressure drag coefficient by increasing the base pressure in the leeward region. This mechanism arises from flow passing through the porous layer, which fills the wake and prevents the formation of a low-pressure suction region. Additionally, the porous structure destabilizes the separated shear layers, promoting energy dissipation and reducing their capacity to form vortical structures. This results in a wider, more stable wake with reduced turbulence intensity, shifted further downstream compared to the bare cylinder. Similar findings have been obtained by Showkat Ali et al., who experimentally demonstrated, by means of PIV (particle image velocimetry), that the presence of porous cover increase the vortex formation length, shifting the outbreak of shedding downstream. The porous coating reduces the momentum deficit in the near wake while maintaining a flatter streamwise velocity profile compared to the bare cylinder. In the far wake, the profiles become narrower, with a larger momentum deficit and sharper slopes due to extended vortex formation. Additionally, the turbulence kinetic energy is significantly lower in both the near and far wake of the coated cylinder, indicating improved flow stabilization. Naito and Fukagata try to explain the stabilization effect due to the porous coating in the wake from two point of view: the dissipation of kinetic energy and the slip velocity within the pores. The dissipation experienced by the flow as it passes through the porous medium is considerably high. Consequently, the fluid loses a substantial amount of energy while traversing the porous coating, and is then ejected downstream of the cylinder. This energy loss leads to the formation of a low-energy, stable region in the wake of the cylinder. In combination with the slip velocity between the pores, this mechanism contributes to stabilizing the shear layers. All the studies analysed above emphasised the connection between the wake-flow stabilization thanks to the pores and noise suppression. However Sato and Hattori tried to provide a more detailed description of reduction of aerodynamic noise by means of DNS at low Re number. Considering values of thickness and permeability that minimized the acoustic power, the incoming flow, when he reaches the cylinder, is spitted into two partes because of the presence of the porous medium: a part of the flow penetrates into the porous medium creating a flow pattern close to that of the jet, while the remining part forms the boundary layer around the cylinder surface. Furthermore part of the flow that previously penetrated inside the pores emerges from within the pores to its outside

forming a thin shear layer which makes a pressure profile characterized by a zero gradient (i.e. constant), this helps to stabilize the flow and suppress the vortex shedding and, as a consequence, leading to an improvement in aeroacoustics performance. Varying the thickness and permeability consistently leads to a reduction in acoustic power and a suppression of unsteady motion. However, the pressure gradient in the wake remains non-zero, meaning the flow is not fully stabilized. From the previously analysed studies, it is evident how complicated it is to thoroughly analyse the flow field within the porous medium, especially when it has a randomized structure. On this purpose J.G. Arcondoulis et al. considered three different porous media: two randomized (metal foam and porous polyurethane) and one structured, with properties similar to the randomized ones. The study revealed that all three porous media demonstrated comparable effectiveness in reducing tonal noise. A further numerical experiment also reveals the strong similarities between the wake structure of the 3-D printer coating and the wake structure of the randomized coating represented by an equivalent Darcy–Forchheimer model. All these similarities allow us to use a structured porous geometry to understand the complex internal flow behaviour of randomized porous coating, which could reveal common behaviours with randomized coatings that are responsible for the noise reduction. A similar work was performed by E.J.G. Arcondoulis et al., who tested a structured porous cover by means of a water tunnel and a water flume for TPIV (Tomographic Particle Image Velocimetry) to understand the basic behaviour of the internal flow in the windward and mid-circumference regions.

Chapter 2: Theoretical background and methodologies

In this section, a theoretical framework is presented to support the understanding of the entire work. Specifically, a brief overview about the acoustic analogies will be provided and then an alternative formulation for this case will be presented through the use of tailored Green's function.

2.1 Introduction to acoustic analogies

The acoustic analogies are obtained through a mathematic rearrangement of the flow-governing equations and they are used to connect the flow itself with the acoustic field aerodynamically generated. They are organised in a way that flow field variables are in the left side of the equation, while on the right side of the equation there are the sources to the acoustic field. The overall operator in the right side is commonly known as wave operator. In the following part of this chapter some useful acoustic analogies for the present work will be briefly analysed.

2.1.1 Lightill's analogy

The first acoustic analogy that it is analysed is the Lighthill's analogy for unbounded flow. The starting point is represented by balance equation of mass and momentum:

$$\frac{\partial \rho}{\partial t} + \frac{\partial}{\partial x_i}(\rho u_i) = 0 \tag{2. 1}$$

$$\frac{\partial}{\partial t}(\rho u_i) + \frac{\partial}{\partial x_j}\left(\rho u_i u_j\right) = \frac{\partial \tau_{ij}}{\partial x_j} \tag{2. 2}$$

Where τ_{ij} are the viscous stresses, ρ is the density and $u_{i,j}$ are velocity components. Applying the time derivative and the divergence operator to the first and second equation, respectively and then subtracting the first from the second:

$$\frac{\partial^2 \rho}{\partial t^2} = \frac{\partial^2}{\partial x_i \partial x_j}\left(\rho u_i u_j - \tau_{ij}\right) \tag{2. 3}$$

At this stage, subtracting from both sides $-c_0^2 \frac{\partial^2 \rho}{\partial x_i \partial x_j} \delta_{ij}$:

$$\frac{\partial^2 \rho'}{\partial t^2} - -c_0^2 \frac{\partial^2 \rho'}{\partial x_i \partial x_j} \delta_{ij} = \frac{\partial^2}{\partial x_i \partial x_j} \left(\rho u_i u_j + (p' - c_0^2 \rho') - \tau_{ij} \right)$$

(2. 4)

Defining the fluctuations respect to a rest medium with constant properties. On the right hand side of 2.4 we retrieve the definition of the Lighthill's tensor defined in first chapter. Since the presence of the operator $\frac{\partial^2}{\partial x_i \partial x_j}$ in the right hand side the source term can be modelled as a quadrupole.

2.1.2 Curle's analogy

Curle' analogy represents an extension of the Lighthill's analogy as it takes into account the effect of the present of the body and their effect on the generation of sound. Given the periodicity of the present problem the equation can be written in the frequency domain. Starting from the equation previously found in the frequency domain:

$$(\nabla^2 - k^2) \hat{\rho}(\boldsymbol{x}, t) = \frac{\partial^2}{\partial x_i \partial x_j} \left(\widehat{T_{ij}} \right)$$

(2. 5)

Where the double time derivative of $\rho' = \hat{\rho} e^{i\omega t}$ and the definition of wavenumber $k = \frac{\omega}{c_0}$ have been substituted. A possible solution of equation 2.5 is given by the convolution product of free field Green's function G_0 in the frequency domain:

$$\hat{\rho}(\boldsymbol{x}, \omega) = \frac{1}{c_0^2} \iiint_V \frac{\partial^2}{\partial x_i \partial x_j} \left(\widehat{T_{ij}} \right) \widehat{G_0}(\boldsymbol{x}|\boldsymbol{y}, \omega) \, d\boldsymbol{y} + \iint_\Sigma \left[\widehat{G_0}(\boldsymbol{x}|\boldsymbol{y}, \omega) \frac{\partial \hat{\phi}}{\partial y_i} - \hat{\rho}(\boldsymbol{y}, \omega) \frac{\partial \widehat{G_0}(\boldsymbol{x}|\boldsymbol{y}, \omega)}{\partial y_i} \right] n_i \, d\Sigma$$

(2. 6)

Where the free field Green's function represents the solution in **x** and time instant t due to a point source placed in **y** that emits at the time instant τ. Substituting the expression of Lighthill's tensor and transferring the double derivate on $\hat{G}$ applying the integration by parts twice:

$$c_0^2\hat{\rho}(\boldsymbol{x},\omega) = -\iiint_V \widehat{T_{ij}} \frac{\partial^2 \widehat{G_0}(\boldsymbol{x}|\boldsymbol{y},\omega)}{\partial y_i \partial y_j}\, d\boldsymbol{y} + \iint_\Sigma \left[\widehat{G_0} \frac{\partial(\hat{p}\delta_{ij} + \rho\widehat{u_i u_j})}{\partial y_i} - (\hat{p}\delta_{ij} + \rho\widehat{u_i u_j}) \frac{\partial \widehat{G_0}}{\partial y_j}\right] n_i\, d\Sigma$$

(2. 7)

Applying the condition of rigid surface $\frac{\partial \hat{p}}{\partial n} = 0$ and the no-slip condition $u_i = 0$, the expression 2.7 becomes:

$$c_0^2\hat{\rho}(\boldsymbol{x},\omega) = -\iiint_V \widehat{T_{ij}} \frac{\partial^2 \widehat{G_0}(\boldsymbol{x}|\boldsymbol{y},\omega)}{\partial y_i \partial y_j}\, d\boldsymbol{y} - \iint_\Sigma \left[\hat{p} \frac{\partial \widehat{G_0}}{\partial y_j}\right] n_i\, d\Sigma$$

(2. 8)

The first term (volume term) is linked to unsteady velocity fluctuations in the wake and it can be modelled as a quadrupole, while the surface term takes into account the effect of the surface in the noise generation. It radiates in the far with a dipolar pattern and it is linked to the pressure fluctuations exerted on the rigid surface. At this stage, in order to evaluate the dependence of the two contributions from the Mach numbers, a proportionality analysis is performed. First of all, let's introduce the far-field approximation:

$$\frac{\partial}{\partial x_j} = -\frac{1}{c_0} \frac{x_j}{|\boldsymbol{x}|} \frac{\partial}{\partial t}$$

(2. 9)

The equation 2.8 becomes:

$$c_0^2\hat{\rho}(\boldsymbol{x},\omega) = \frac{1}{c_0^2} \frac{x_i x_j}{|\boldsymbol{x}|^2} \frac{\partial^2}{\partial t^2} \iiint_V \widehat{T_{ij}}\, \widehat{G_0} dV + \frac{1}{c_0} \frac{x_j}{|\boldsymbol{x}|} \frac{\partial}{\partial t} \iint_\Sigma \hat{p} \widehat{G_0}\, d\Sigma$$

(2. 10)

Defining the following proportionality rules:

$$\frac{\partial}{\partial t} \sim \frac{U}{D} \quad , T_{ij} \sim \rho U^2 \, , \iiint_V . \sim D^3 \, , \iint_\Sigma . \sim D^2$$

Where U and D are characteristic velocity and dimension of the problem respectively. Isolating the quadrupolar and dipolar contributions:

$$\hat{\rho}_{quadr} \sim D^3 \, \rho U^4 \frac{1}{c_0^2} \sim M^4$$

$$\hat{\rho}_{dip} \sim D^2 \, \rho U^3 \frac{1}{c_0} \sim M^3$$

(2. 11)

Substituting the relationship for the pressure fluctuations on the surface $p \sim \rho U^2$. As a result, at low Mach numbers the dipolar contribution dominates over the quadrupolar one.

2.1.3 Tailored Green's function

The acoustic sources retrieved in the previous section in the Curle's analogy formula must be intended as equivalent sources. As stated in previous section aerodynamic noise of a circular cylinder can be modelled as a quadrupole volume source scattered on the surface. Following the notation of Gloerfelt et al. a new formulation based on the introduction of a tailored Green's function is proposed. A bidimensional approach is used to obtain a good representation of flow-topology, even if, downstream the cylinder, the flow is intrinsically 3-D. Starting from the formula of the acoustic pressure with a generic Green function in the frequency domain:

$$c_0^2 \hat{\rho}(\boldsymbol{x}, \omega) = - \iiint_V \widehat{T_{ij}} \frac{\partial^2 \hat{G}(\boldsymbol{x}|\boldsymbol{y}, \omega)}{\partial y_i \partial y_j} \, d\boldsymbol{y} - \iint_\Sigma \left[\hat{p} \frac{\partial \hat{G}}{\partial y_j} \right] n_i \, d\Sigma$$

(2. 12)

Substituting the free-field Green's function Curle's analogy formula can be retrieved. However, let's consider a tailored Green's function in the frequency domain $\widehat{G_1}$ which satisfies a certain boundary condition on Σ. The equation 2.12 becomes:

$$c_0^2 \hat{\rho}(\boldsymbol{x}, \omega) = - \iiint_V \widehat{T_{ij}} \frac{\partial^2 \widehat{G_1}(\boldsymbol{x}|\boldsymbol{y}, \omega)}{\partial y_i \partial y_j} \, d\boldsymbol{y} - \iint_\Sigma \left[\hat{p} \frac{\partial \widehat{G_1}}{\partial y_j} \right] n_i \, d\Sigma$$

(2. 13)

For an hard surface $\frac{\partial \widehat{G_1}}{\partial n} = 0$, consequently the surface term of above equation becomes zero. The acoustic pressure can be expressed only as a function of a volume integral. Such tailored Green's function can be constructed adding a term $\widehat{G_s}$, which satisfied the imposed boundary condition and accounts for the scattering mechanisms on the surface,

to the free-field Green's function $\widehat{G_0}$. At this stage, subtracting the equation 2.13 from 2.8, the following equivalence is satisfied:

$$\iiint_V \widehat{T_{ij}} \frac{\partial^2 \widehat{G_s}(\boldsymbol{x}|\boldsymbol{y},\omega)}{\partial y_i \partial y_j} = \iint_\Sigma \left[\hat{p}\frac{\partial \widehat{G_0}}{\partial y_j}\right] n_i \, d\Sigma$$

(2. 14)

This inform us that the dipolar term of the Curle's analogy physically corresponds to the counterpart of the aerodynamic noise produced in the wake which is then scattered on the surface. In this way, since the scattered contribution is characterized by a dipolar directivity, a quasi-dipolar radiation pattern is retrieved in the far-field.

2.1.4 Ffowcs Williams – Hawkings's analogy

The Lighthill-Curle's analogy was further extended accounting for the arbitrary motion of surfaces within the domain. Such situation is spatially inhomogeneous, in order to retrieve the spatial homogeneity, an infinite extension of the acoustic medium is considered, the presence of rigid bodies is taken into account by "mathematical surfaces" that perfectly matches the real surfaces. As a result the motion outside and on these mathematical surfaces is identical to the real motion, while the motion inside the bodies can be chosen arbitrarily. In this case a zero acoustic field is considered. Consequently the external flow value does not match the value at the boundaries leading to the formation of discontinuities on such surfaces. To restore the spatial homogeneity mass and momentum acoustic sources have to be introduced, whose effect is equivalent to that of the surfaces.

Let's consider a rigid surface Σ that enclose all moving bodies, the zero acoustic field is obtained through the following mathematical formalism:

$$H(g) = \begin{cases} 0 & inside\ \Sigma \quad (\mathrm{g} < 0) \\ 1 & outside\ \Sigma \quad (g > 0) \end{cases}$$

(2. 15)

While the function g is zero on the surface and it satisfies the condition $\frac{Dg}{Dt} = 0$. Multiplying the equations 2.1 and 2.2 for the weight function $H(g)$:

$$\begin{cases} H(g)\left(\frac{\partial \rho}{\partial t} + \frac{\partial}{\partial x_i}(\rho u_i)\right) = 0 \\ H(g)\left(\frac{\partial}{\partial t}(\rho u_i) + \frac{\partial}{\partial x_j}(\rho u_i u_j) - \frac{\partial \tau_{ij}}{\partial x_j}\right) = 0 \end{cases}$$

(2. 16)

Since the derivative of the weight function H(g) is the Dirac delta $\delta(g)$, for the chain rule, its time and spatial derivative are:

$$\frac{\partial H}{\partial t} = \delta(g)\frac{\partial g}{\partial t}, \quad \frac{\partial H}{\partial x_i} = \delta(g)\frac{\partial g}{\partial x_i}$$

(2. 17)

At this point, the mass balance equation in 2.16 becomes:

$$\frac{\partial}{\partial t}[(\rho - \rho_0)H] + \frac{\partial}{\partial x_i}[\rho u_i H] = (\rho - \rho_0)\frac{\partial H}{\partial t} + u_i \rho \frac{\partial H}{\partial x_i}$$

(2. 18)

Here, ρ_0 represents the reference density, which is considered constant. By substituting both expressions into equation 2.17 and applying the condition of a zero material derivative:

$$\frac{\partial}{\partial t}[(\rho - \rho_0)H] + \frac{\partial}{\partial x_i}[\rho u_i H] = \left[\rho(u_i - U_i) + \rho_0 U_i\right]\frac{\partial g}{\partial x_i}\delta(g)$$

(2. 19)

Where U_i is the convective velocity. From 2.19, it can be noted that, writing the continuity equation as a function of variables that vanishes inside the surface leads to appearance of a source term in the right hand side on the surface (thanks to the presence of $\delta(g)$), which can interpreted as a mass source. Performing the same steps with the momentum balance equation :

$$\frac{\partial}{\partial t}[\rho u_i H] + \frac{\partial}{\partial x_j}\left[(\rho u_i u_j - \tau_{ij} - p_0 \delta_{ij})H\right] = F_i \delta(g)$$

(2. 20)

Where the right hand side term can be written as:

$$F_i = u_i Q_m + \rho_0 f_i$$

(2. 21)

And it can be interpreted as a momentum source localized on the surface and Q_m is the right-hand side of the mass balance equation. Applying the time derivative to the equation 2.19 and the divergence operator to the equation 2.20:

$$\frac{\partial^2}{\partial t^2}((\rho - \rho_0)H(g)) = \frac{\partial}{\partial t}[Q_m \delta(g)] - \frac{\partial}{\partial x_i}[F_i \delta(g)] - \frac{\partial^2}{\partial x_i \partial x_j}\left[(\rho u_i u_j - \tau_{ij} - p_0 \delta_{ij})H(g)\right]$$

(2. 22)

Subtracting from both sides $c_0^2 \frac{\partial^2}{\partial x_i \partial x_j}[\rho' H(g)]$:

$$\frac{\partial^2}{\partial t^2}(\rho' H(g)) - c_0^2 \frac{\partial^2}{\partial x_i \partial x_j}\left[\rho' H(g)\right] = \frac{\partial}{\partial t}[Q_m \delta(g)] - \frac{\partial}{\partial x_i}[F_i \delta(g)] + \frac{\partial^2}{\partial x_i \partial x_j}\left[T_{ij} H(g)\right]$$

(2. 23)

When the surface is absent, g>0 everywhere and H(g)=1, and the Lighthill's analogy is retrieved. A general solution of equation 2.23 is given by the convolution with the free-field Green's function:

$$H(g)c_0^2 \rho'(\boldsymbol{x}, t) = \frac{1}{4\pi}\frac{\partial^2}{\partial x_i \partial x_j}\iiint_V \left[\frac{T_{ij}}{R|1 - M_\Sigma cos\theta|}\right] dV - \frac{1}{4\pi}\frac{\partial}{\partial x_i}\iint_\Sigma \left[\frac{F_i}{R|1 - M_\Sigma cos\theta|}\right] n_j d\Sigma + \frac{1}{4\pi}\frac{\partial}{\partial t}\iint_\Sigma \left[\frac{Q_m}{R|1 - M_\Sigma cos\theta|}\right] n_i d\Sigma$$

Where the terms in square brackets means that they are evaluated at the retarded time $\tau = t - \frac{R}{c}$, R is the distance between source and observer, θ is the angle between source and observer and finally $(1 - M_\Sigma cos\theta)^{-1}$ is the factor of convective amplification where Mach number M_Σ is based on the velocity of surface. The input for the far-field calculations is given by flow-field data coming from a surface measurement file. During the present work two different FW-H formulations will be considered:

- **FW-H solid:** uses a standard measurement surface file and require the pressure variable on such surface. It accounts only for the scattered acoustic sources.

- **FW-H permeable:** uses a sample face measurement as input file and it requires pressure, velocity components and density variables. It considers both direct and scattered acoustic source.

The concept of sampled face and standard measurement file will be clarified in the following chapter where the computational set-up will be described. The far-field analysis will be performed with the commercial software PowerAcoustic 2025 where the formulation 1A developed by Farassat and Succi is implemented.

2.2 Methodologies

In the second part of this chapter, the methodologies employed throughout the project are described. The first section specifically addresses the computation and selection of spectral parameters related to the Power Spectral Density (PSD) of both near-field and far-field pressure signals. While in the second part a theoretical background about Spectral Proper Orthogonal Decomposition (SPOD) is provided together with the choice of spectral parameters for this analysis.

2.2.1 Post-processing parameters

The acoustic pressure is recorded at a sampling frequency of 30 kHz for both formulations. The power spectral density is estimated using Welch's method, with a window size of 2^12 samples and 50% overlap, resulting in a frequency resolution of 7 Hz. The PSD values are referenced to a pressure of $p_o = 20\ \mu Pa$ as follows:

$$\mathrm{L}_p = 10 log_{10}\left(\frac{\phi_p}{p_0^2}\right)$$

(2. 24)

To retrieve the directivity of the acoustic field the overall sound pressure level is computed as follows:

$$L_{p,0} = 10\ log_{10}\left(\sum 10^{\frac{L_p}{10}}\right)\ dB$$

(2. 25)

Furthermore, to gain a deeper understanding of the contributions of scattered and direct sources to the far-field pressure, the coherence between the far-field pressure and the near-

field pressure, as well as the coherence between the far-field pressure and velocity fluctuations, is computed as follows:

$$\gamma_{a,b}^2 = \frac{|\phi_{a,b}(f)|^2}{\phi_{a,a}(f)\phi_{b,b}(f)}$$

(2. 26)

Where a and b are two generic signals in the time domain that can be replaced by velocity fluctuations and far-field pressure for instance. $\phi_{a,b}(f)$ is the cross-spectrum of the signals in the frequency domain, $\phi_{a,a}(f)$, $\phi_{b,b}(f)$ are their power spectral densities.

2.2.2 SPOD theoretical background

In order to better understand the theory about the SPOD, a brief introduction will be provided. For further details, the reader is referred to Schmidt and Colonius 2020. Developed in the recent years, SPOD is an innovative method to extract coherent structures from flow data. The idea of this method id to find an optimal orthogonal basis (i.e. modes) that captures the largest possible amount of energy from the data. The difference with the most commonly used POD is that such modes are orthogonal both in space and in time. Here the focus is on the Welch's method of the discrete form of SPOD, that is the method on which the specific function Matlab "*spod*" is based on. The procedure is the same to that used to compute the PSD of a simple time series of data. Let us consider a two-dimensional domain discretized by a grid of points, where data have been sampled at each point over N_t time frames. This dataset is then divided into N_{blk} blocks or snapshots. Each block contains N_{FFT} snapshots, with an overlap of N_{ovlp} snapshots between consecutive blocks. To have a clearer idea, let's imagine to deal with a series of slices, each of them represents the data sampled in the points considered at a generic time step. Such blocks are first Fourier transformed according to the following formula:

$$\widehat{v_m}^{(k)} = \sum_{k=0}^{N_{FFT}-1} v^{(k)}(t_{j+1})\, e^{-i2\pi jm/N_{FFT}}, \quad k = \frac{-N_{FFT}}{2} + 1, \dots, \frac{N_{FFT}}{2}$$

(2.27)

Where v is the variable sampled, j a generic instant, m is the frequency index and k is the time frame index. The Fourier transformed blocks are then reordered by frequency. After

that the remaining analysis is performed for every frequency. First of all, the $\hat{Q}$ matrix is constructed as follows:

$$\hat{Q} = \begin{bmatrix} \vdots & \vdots & \vdots \\ \widehat{q_1} & \widehat{q_2} & \dots \widehat{q_{N_t}} \\ \vdots & \vdots & \vdots \end{bmatrix} \qquad \hat{Q} \in \mathbb{R}^{MxN_t}$$

(2.28)

Where M is the number of spatial points and N_t is always the number of snapshots. At this stage the Cross Spectral Density (CSD) matrix $\hat{C}$ is computed:

$$\hat{C} = \frac{1}{N_t - 1} \hat{Q}\hat{Q}^T$$

(2.29)

Then SPOD modes and eigenvalues are computed:

$$\hat{C}W\hat{\Phi} = \hat{\Phi}\hat{\Lambda}$$

(2.30)

Where $\hat{\Phi}$ is a matrix with the same dimensions of $\hat{Q}$, whose columns represent SPOD modes and $\hat{\Lambda}$ is diagonal matrix whose values are the eigenvalues of the CSD matrix. It is reminded that all these passages must hold for every frequency. Finally W is the weight matrix, whose choice determines the optimality and orthogonality of modes. As a result the SPOD modes are, from a mathematical point of view, the eigenvectors of CSD matrix $\hat{C}$.

2.2.3 Choice of SPOD spectral parameters

In this sub-section the choice of the spectral parameters, such as N_{ovlp}, N_{FFT}, f_s, will be explained and justified in order to obtain an accurate estimation of CSD matrix $\hat{C}$. The time step Δt, that is temporal distance between two consecutive snapshots, is fixed from the simulation and it is equal to 3.3912 x 10^{-5} s. Consequently the sampling frequency f_s is fixed as well:

$$f_s = \frac{1}{\Delta t} \cong 30\ kHz$$

(2.31)

The maximum resolvable frequency is given by Nyquist condition:

$$f_{max} = \frac{f_s}{2} \cong 15\ kHz$$

(2.32)

The window's width N_{FFT} must be chosen considering two different constrains. The first one is frequency resolution given by:

$$\Delta f = \frac{f_s}{N_{FFT}}$$

(2.33)

In this case a relatively large window is required not to obtain a biased spectrum, where contributions at different nearby frequencies are spread over the frequency bin. However, when Welch's method is applied, if we select a large N_{FFT} value, we will end up with fewer segments in the dataset, which means the resulting spectrum may not achieve good statistical convergence. The number of total blocks N_{blk} is defined as follows:

$$N_{blk} = floor\left[\frac{N_t - N_{ovlp}}{N_{FFT} - N_{ovlp}}\right]$$

(2.34)

For the present case a window's width (i.e. N_{FFT}) of 2^{10} is considered. As a result a frequency resolution of 28.80 Hz is achieved. Moreover a 50% overlap (or $N_{FFT}/2$) is taken, because with this value the uncertainty of the estimate of PSD is minimized and greater values do not lead to better results. A total of 5000 frames is considered for the present analysis, which correspond to a physical time of 0.17 s and 12 vortex shedding cycles. Consequently a number of segments (i.e. modes) N_{blk} of 8 are statistically converged. Finally, when algorithm described in the previous section is applied to non-periodic data, the problem of the spectral leakage occurs. Indeed the non-periodicity introduces some discontinuities that distorts the spectrum. To alleviate this effect, each block is multiplied by a temporal window that makes the data periodic in every segment. In the function "*spod"* in Matlab, such window is the Hanning window:

$$w(j) = 0.54 - 0.46\ cos\left(\frac{2\pi j}{N_{FFT} - 1}\right) \quad with\ j = 0, 1, \ldots., N_{FFT} - 1$$

(2.35)

Since such window the overall spectrum is altered, the Fourier's transform of the windowed data are multiplied by a coefficient a_w, which is equal to 2 for the Hanning window, to partly alleviate this effect.

2.3 Basic principles of Lattice-Bolzmann Method

In the following section a brief overview of Lattice-Boltzmann-methods will be provided on which the commercial software PowerFLOW 2025 is based. They represent a discretised approach to solve Boltzmann equation and an alternative to the most commonly used CFD methods based on Navier-Stokes equations.

2.3.1 Discrete Boltzmann equation

Starting from the Boltzmann equation in continuous form:

$$\frac{\partial f}{\partial t} + \vec{u}\frac{\partial f}{\partial \vec{x}} + \vec{F}\frac{\partial f}{\partial \vec{u}} = \Omega$$

(2. 36)

Where the function $f(t, \vec{x}, \vec{u})$ represents the probability of finding a particle located within the spatial interval $[\vec{x}, \vec{x} + \Delta\vec{x}]$, the time interval $[t, t + \Delta t]$ and having a microscopic velocity $[\vec{u}, \vec{u} + \Delta\vec{u}]$. The first term of equation 2.24 is time variations of f, the second one represents the spatial variations and last one the effects of external forces which will be neglected for the remaining discussion. The right-hand side term is the collision operator which is responsible for altering the distribution function due to interactions and collisions between particles. Writing the above equation in discrete form and assuming $\Delta\vec{x} = \Delta t = 1$:

$$\frac{f_i(t + \Delta t, \vec{x} + \Delta\vec{x}) - f_i(t, \vec{x})}{\Delta t} = \Omega_i$$

(2. 37)

We have just stated that in discrete Lattice-Boltzmann method the particles exists in discrete space location, at discrete intervals of time and they can move in discrete directions with discrete values of velocity. They reside in a cubic lattice, which consists of voxels, which are basic 3D volume elements. The particles are able to travel from one

voxel to another within a timestep. Additionally, the lattice includes surfels, surface elements that appear in the zones where the fluid intersect the solid body.

2.3.2 Velocity models

Since the Lattice-Boltzmann method is only a simplification of Boltzmann equation, the velocity of particles can assume only a discrete number of directions and values, on this regard the DkQb notation have been introduced, where k denotes the spatial dimension and b indicates the number of discrete velocity directions. In the following figure the D3Q19 model is reported.

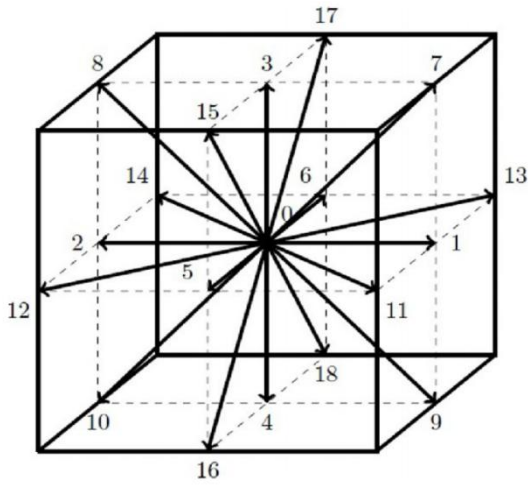

Figure 2.1 *D3Q19 model (taken from Zhang et al. 2006)*

For practical uses, we are more interested macroscopical variables than the probability function f. The former can be retrieved by integrating the probability function in all velocity directions. For instance density and momentum can be obtained:

$$\rho(t,\vec{x}) = \int_{-\infty}^{\infty} f(t,\vec{x},\vec{u})d\vec{u} = \sum_{i=0}^{b} f_i$$

$$I = \rho(t,\vec{x})u(t,\vec{x}) = \sum_{i=0}^{b} f_i\,\vec{u}$$

(2. 38)

In this way starting from Boltzmann equations based on a microscopic description of gas kinetic, the equations in macroscopic form can be derived through the Chapman-Enskong expansion. By expanding the distribution function around its equilibrium value in powers

of Knudsen number, which the ratio between the mean free path of particles with respect to a physical length scale:

$$f = f^{(0)} + \varepsilon f^{(1)} + \varepsilon^2 f^{(2)} + \cdots$$

(2. 39)

Substituting the equation 2.27 into equations 2.26 the macroscopic variables can be retrieved. For density and momentum the equilibrium state of distribution function is enough, while for higher order moment non-equilibrium states have to be taken into account.

2.3.3 Computational loop

In order to simulate the behaviour of the real fluid, the particles are able to interact and to move from one voxel to another during a timestep. Every time step is composed by two different phases:

- **Move phase:** the particles move from one voxel to an adjacent one (timestep 1a in figure 2.2). The state in this phase is obtained from the previous step through the following equation:

$$f_i(\vec{x} + e_i, t + \Delta t) = f_i(\vec{x}, t)$$

(2. 40)

This states the population moving in direction e_i coming from position $\vec{x}$ at time instant t that arrive in position $\vec{x} + e_i$ at time instant $t + \Delta t$. It represents the intermediate step between propagation and collision.

- **Collision phase:** particle in the same voxel collide, they change their velocity and direction, conserving mass, momentum and energy within the voxel. This process is governed by LBM equation written in general form:

$$f'_i(\vec{x}, t) - f_i(\vec{x}, t) = \Omega_i$$

(2. 27)

Where $f'_i(\vec{x}, t)$ is the new state post-collision. The main goal of the collision phase is to recover thermodynamic equilibrium at an appropriate rate. The whole procedure is explained in the following figure.

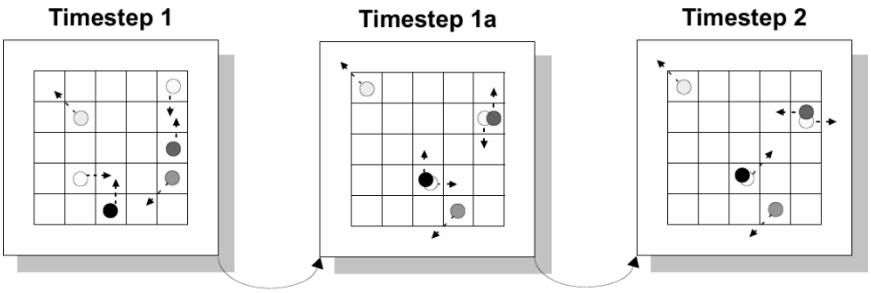

Figure 2.2 *Phases of computational loop*

Regarding the voxel-surfel advection the particles, as soon as the particles hit the surface, they are captured in the surface as well. During this collision the exchange of energy and momentum is allowed in order to satisfy the boundary conditions, while the conservation of mass is enforced. After this process they are reflected and they recover their position in the fluid voxels.

2.3.4 The BGK collision operator

Let's focus on the collision operator Ω, that appears in the right hand side of Bolzmann equation. In particular the Bhatnagar-Gross-Krook operator is considered. A relaxation time is introduced, during which the probability density function gradually returns to its equilibrium state. In discrete form it can be written:

$$\Omega_i = \frac{-1}{\tau}\left(f_i - f_{i,eq}\right)$$

(2. 28)

Where τ is the relaxation time. As a result the whole equation in discrete form becomes:

$$f_i(t + \Delta t, \vec{x} + \Delta\vec{x}) - f_i(t, \vec{x}) = \frac{-\Delta t}{\tau}\left(f_i - f_{i,eq}\right)$$

(2. 43)

The ratio $\frac{\Delta t}{\tau}$ can be seen as the frequency of collision. The change in the probability density function is proportional to the deviation of the distribution function from its equilibrium value, that is given by the Maxwell-Boltzmann equilibrium distribution.

Chapter 3: Computational set-up

In this section the complete numerical setup used for the simulation will be described. The commercial software PowerCASE 6-2025 has been employed to configure the simulation case, specifying the type of simulation, boundary conditions, resolution regions, and other relevant parameters. The outcome of this setup is a *.cdi* file, which will subsequently be used as input for the discretization and simulation processes performed with the commercial software PowerFLOW 6-2025. Moreover a description of geometry and porous coating considered for this case will be provided.

3.1 Steps of setting up the PowerFLOW problem

In this subsection the various steps of setting up the simulation case will be analysed following the way provided by the PowerCASE user's guide. Actually, many steps will not be examined as they refer to cases that fall outside the scope of the present context.

3.1.1 Flow solver

First of all, the simulations options have to be defined. They include the dimensionality of the problem, which is set to 3D. The simulation fluid and flow type are set to ideal gas and external respectively. Since we deal with a relatively high Reynolds number (the frees stream velocity is 30 m/s) the simulation method is set to turbulence model which is employed to both bulk fluid and near wall. In turbulence modelling, the smaller, unresolved scales of motion are represented through models that rely on the fundamental principles of turbulent fluid dynamics. Specifically, PowerFLOW employs Very Large Eddy Simulations (VLES), directly capturing the most energetic flow structures while modeling the smaller, unresolved scales. This approach is based on use of the state of art renormalization group form of the $k-\varepsilon$ equations. The influence of unresolved scales on the resolved ones is accounted for through eddy viscosity and the turbulent Prandtl number. In the voxels nearest to the surface, the velocity field is assumed to follow the universal, geometry-independent Law of the Wall, as illustrated in the following figure.

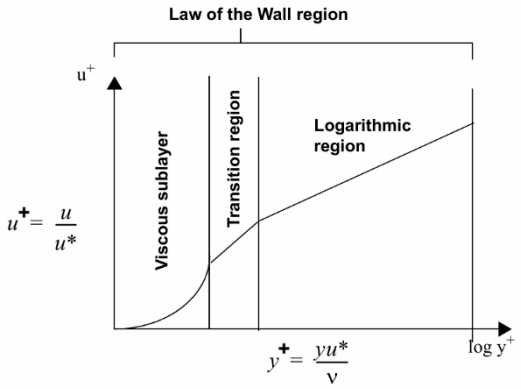

Figure 3.1 *Law of the Wall*

The Mach regime is set to low (M<0.5). The discretization has been performed by means of D3Q19 velocity model introduced in the previous chapter. The macroscopic flow variables are retrieved integrating over 19 discrete directions using a third-order truncation Chapman-Enskog expansion. Finally the collision model based on Bhatnagar-Gross-Krook is used.

3.1.2 Geometry and porous medium properties

The geometry for the present case is simply imported in a *.stl* file, which contains the bare cylinder and 4 different layers of small cylinders arranged around the bare one that compose the structured porous medium. The diameter of the bare cylinder is 40 mm, while the diameters of the small cylinders are d_4=0.417 mm (outermost layer), d_3=0.417 mm, d_2=0.350 mm and d_1=0.321 mm (innermost layer). They are wrapped and equally spaced by 5° around the solid cylinder obtaining a total of 72 small cylinders for each layer. The thickness of the porous coating is h/d = 0.25 (d is bare cylinder diameter).

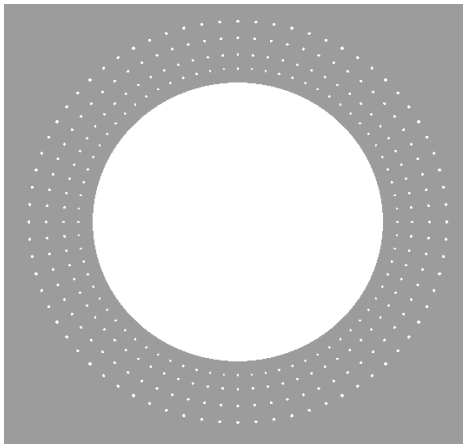

Figure 3.2 *Structured porous coating*

The overall porosity is 98%, defined as the ratio of porous medium volume with respect to an equivalent solid. Since it is proved that this configuration has the best properties in terms of noise reduction (Wen et al. 2021). The origin reference system considered is fixed in the centre of cylinder, the X-axis is in the streamwise direction (flow goes from left to right according figure 3.2), the Y-axis is in the crosswise direction and finally the Z-axis in the spanwise direction. The simulation domain is a parallelepiped with dimensions 42.75 *d* x 31.75 *d* x 0.25 *d*.

3.1.3 Global parameters

In this section some global parameters that control the overall behaviour of the simulation will be defined. All these parameters will then be used by PowerViz to compute the various quantities in dimensionless form (pressure coefficient, forces coefficients etc.). For an external flow, like the present case, the free-stream values are considered:

- **Characteristic pressure:** 1 atm
- **Characteristic density:** 1.225 kg/m^3
- **Characteristic velocity:** 30 m/s
- **Characteristic temperature:** 288.5 K
- **Characteristic viscosity:** 1.46e-5 m^2/s
- **Characteristic length:** 40 mm
- **Characteristic area:** 0.0004 m^2

The resolution, which is the size of voxels/surfels along the characteristic length, is set to 2048. This value represents also the voxel size in the finest scale of resolution. In this

case, the characteristic length coincides with bare diameter, the minimum voxel size is 1.95e-5 m. The simulation time is the amount of physical time we want to simulate (not the time that the computer will take to perform the simulation) is set to 0.4 s which corresponds to about 45 vortex shedding cycles. The data are saved after a transient of 0.16 s. The simulation time is discretized into discrete intervals called timestep.

3.1.4 Variable resolution regions

The concept of variable resolution regions involves adjusting the voxel resolution based on the area of interest. Specifically, in external flows, the largest gradients are typically found near the surface. Therefore, the finest grids are required in these areas to accurately capture these gradients and the data need to be saved every timestep. As we move away from the surface, lower gradients are expected. Therefore, the voxel size can be increased, and the data can be updated at larger timestep intervals. As a result the overall voxels number is reduced leading to beneficial effects in terms of computational cost. Firstly, to establish these variable resolution regions, it is necessary to generate distinct geometric shapes of progressively increasing dimensions and subsequently assign a specific resolution level to each. In this case four different cylinder of increasing diameters are and four different boxes of increasing dimensions are generated. Then the highest level of resolution is assigned to the smallest cylinder (which is obviously greater than the bare cylinder) and lowest level is assigned to the biggest box previously defined. As we move from one resolution region to the following one, the voxel size doubles and the update frequency halves. In the following table all the resolution region considered are summarized.

Shape	Dimensions	Voxel size [m]	Update frequency [Hz]	Level of resolution
Cylinder	1.26 *d*	1.95*e*-5	3.*02e*+*7*	7
Cylinder	1.575 *d*	3.91*e*-5	1.51*e*+*7*	6
Cylinder	1.875 *d*	7.81*e*-5	7.549*e*+*6*	5
Cylinder	2.325 *d*	1.56*e*-*4*	3.775*e*+*6*	4
Box	8.25*d* x 4.5*d*	3.13*e*-*3*	1.887*e*+*6*	3
Box	13.5*d* x 7.5*d*	6.25*e*-*4*	9.436*e*+*5*	2
Box	21*d* x 10.5*d*	1.25*e*-*3*	4.718*e*+*5*	1
Box	25.5*d* x 13.5*d*	2.50*e*-*3*	2.359*e*+*5*	0

Table 1 *Resolution scales*

The various resolution regions share the same spanwise dimension, which is equal to that of the solid cylinder. Their minimum thickness is set to 8 local voxels.

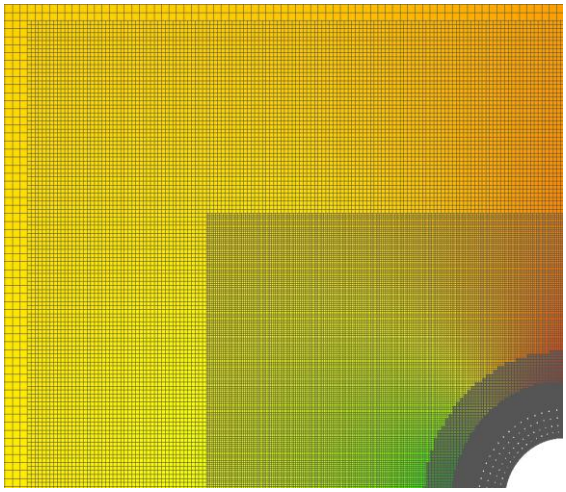

Figure 3.1 *Resolution regions*

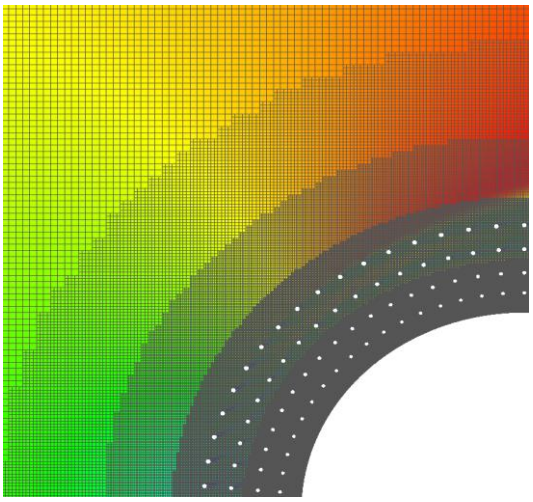

Figure 3.2 *Detail of resolution regions*

3.1.5 Boundary conditions

Before applying the boundary conditions, it is essential to first define the geometry and distinguish the boundaries of the simulation domain. The inlet, outlet, top, and bottom surfaces should be treated as solid components, while the entire simulation volume is considered as the fluid region. Additionally, the initial static pressure and velocity at timestep 0 must be specified according to the values set in the global parameters tab.. Boundary conditions are enforced on all sides of the computational domain. At the inlet, both static pressure and velocity are specified according to the values defined in the global parameters. The free-stream velocity is aligned with the X-axis. While for top, bottom and outlet side only a condition on static pressure is imposed. The no-slip condition is applied to all solid boundaries. Finally an acoustic buffer characterized by high viscosity is defined at a distance of *32d* from the centre of cylinder to prevent the reflection of acoustic waves on the boundaries. Boundary conditions imposed are summarised in the following figure.

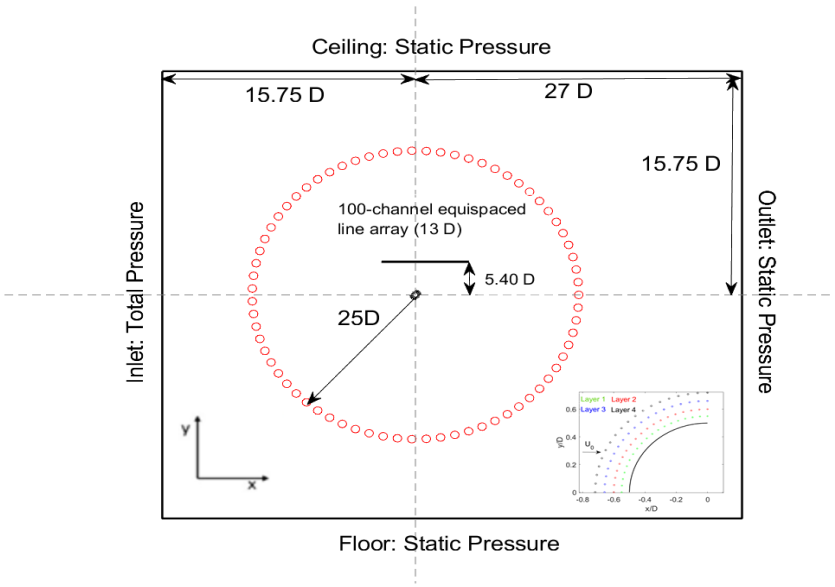

Figure 3.3 *Boundary conditions and size of simulation volume*

3.1.6 Measurement windows

In this tab we are able to define which data can be recorded during the simulation according to the methods proposed by PowerCASE. For this case following measurement windows are defined:

- **Standard Measurement by Region,** enables data storage within the volume defined by a specific part. In this case two different windows are defined to save both instantaneous and mean data in the simulation volume. The 'Instflow' window records pressure, velocity, and density at a sampling frequency of 30 kHz, capturing instantaneous values. In contrast, the 'Meanflow' window stores the same variables at a sampling frequency of 2.5 Hz, meaning the data are averaged over the entire simulation duration, capturing the mean values. For the two windows both surface file .snc and fluid file .fnc will be generated.
- **Standard Measurement by Face,** records variables on the prescribed faces. The window named ‘FWH_solid’ records pressure, velocity, density and forces on the cylinder surface. The output will be a surface file (i.e. FWH_solid.snc), that will be employe as input for far-field computations with FWH solid formulation.
- **Sample Face Measurement:** This feature records data on non-solid faces that do not affect the overall flow behaviour. In this case, the selected faces belong to a parallelepiped with dimensions 22.5d×12d×0.25d. The window, named *FWH_Perm*, saves density, pressure and velocity and generates a surface file as output, which will be used for far-field computations based on the FWH permeable formulation.
- **Composite Measurement by Face:** Records integrated value on a surface, it does not provide information about the spatial variations of variables. For this case it is used for saving the forces acting on the cylinder surface.

3.1.7 Step of simulation

After completing all the aforementioned steps, the .cdi file is generated and used as input for the simulation. This process can be further divided into three additional steps:

- **Discretizer:** it discretizes the simulation volume into surfels and voxels, taking as input the *.cdi* file.
- **Decomposer:** It divides a case into multiple parts for parallel simulation on a multiprocessor server. At the end the *.lgi* will be generates
- **Simulator:** performs the simulation and generates the results.

Chapter 4: Aeroacoustic results

In this chapter the sound pressure levels of the far-field data are computed in the frequency domain using both solid and permeable formulation. The analysis will focus mostly on the low frequency noise, which is the main topic of the present work. However, a quick reference will be made about the high-frequency noise and its generation mechanism.

4.1 Far-field pressure spectra

The following figure illustrates the sound pressure level as a function of the Strouhal number based on the bare diameter and free-stream velocity considering a microphone placed at (0,1,0) [m] according to the reference system presented in the second chapter (i.e. x/d = 0 and y/d = 25 in figure 3.3).

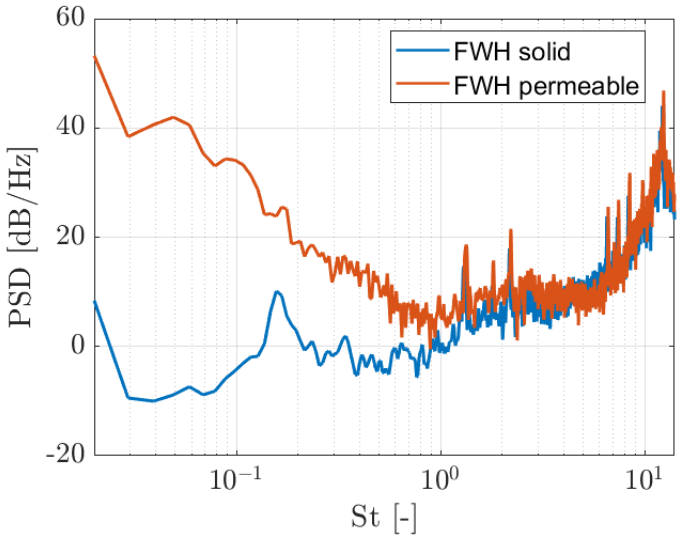

Figure 4.1 *Sound Pressure Level with microphone placed at (0,1,0) [m]*

In the low-frequency range, the FWH permeable formulation, which incorporates both direct and scattered acoustic sources, exhibits a greater contribution compared to the FWH solid formulation, which considers only the scattered acoustic source (i.e., dipolar acoustic source). Then for St > 1, the discrepancy between the two contributions tends to decrease and the two formulations provide the same contribution. However in the high frequency range the sound generation mechanism is different and it will be briefly

analysed later. This result informs us that, despite the low Mach number of the present case, at low frequencies the acoustic field is dominated by quadrupolar source in the wake, while the dipolar source provides a negligible contribution. As a result, after the experimental studies conducted by Zamponi et al. 2024, the relevance of the quadrupolar source is confirmed also by numerical results. Another aspect to underline is that for the permeable formulation there is no trace of tonal peak, because the contribution of the face of the parallelepiped hit by the wake have not been considered, consequently the effect of the oscillatory movement of large scale vortices has been removed.

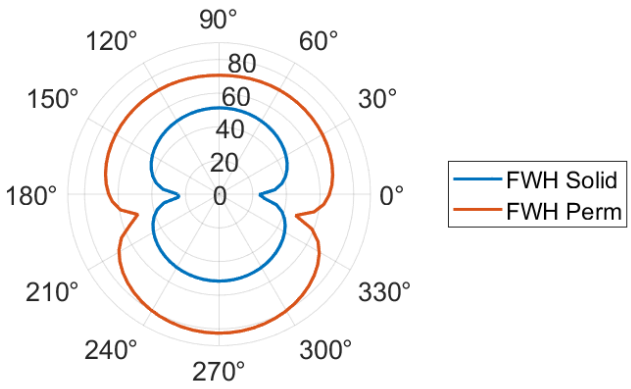

Figure 4.2 *Directivity acoustic field up to St=1*

In the figure 4.2 the overall sound pressure level is plotted, considering an array of microphones arranged on a radial pattern of 1 m from the centre of the cylinder equally spaced with an angle of 5° (the red points reported in figure 3.3). The integration have been performed up to St = 1, where the two formulations provide a distinct contribution. The dominance of permeable formulation with a gap of more than 20 dB between the two curves. Despite the relevance of the quadrupolar sources, a quasi-dipolar acoustic field is retrieved in the far field confirming the results found by Zamponi et al. 2024. A physical interpretation of these results will be elucidated in the next chapter where the effects of the porous coating on the wake's pattern and their repercussions on the aeroacoustic perspective will be analysed.

4.2 Band-pass filter approach

An initial investigation of the acoustic field generated by the structured porous-coated cylinder can be carried out by applying a band-pass filter to the pressure field, with particular attention to both low- and high-frequency regimes. Subsequently, a physical explanation will be provided to clarify why this approach yields meaningful results only in the high-frequency range.

4.2.1 Low-frequency range

Starting from the low-frequency range a band-pass filter is applied to the pressure field from 75 Hz to 450 Hz (i.e. from St = 0.1 to St = 0.6) and a generic time frame is reported in the figure below.

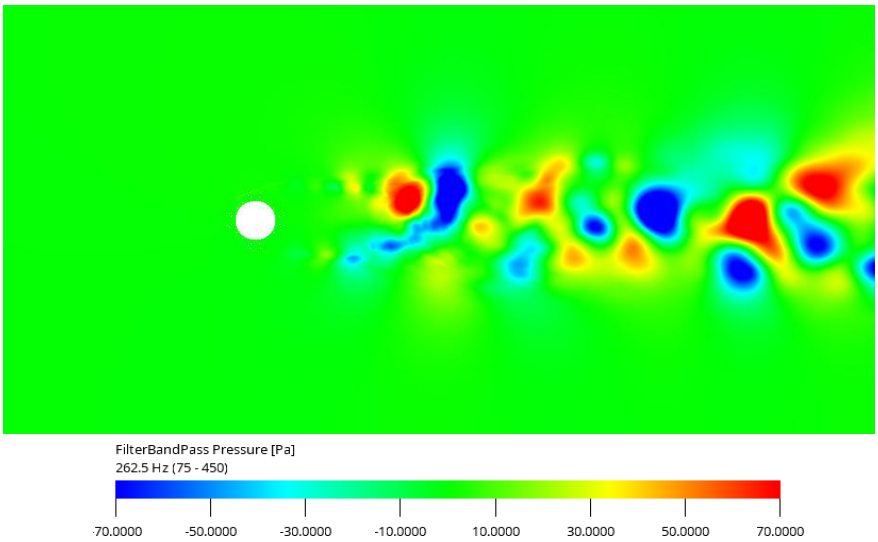

Figure 4.3 *Band-pass filter pressure 75-450 Hz*

It is evident that the hydrodynamic contribution predominates throughout the entire field, primarily due to the presence of large-scale structures in the wake. These structures exhibit significantly greater amplitude compared to the acoustic components, thereby rendering the latter negligible in comparison. In other words, the acoustic component is overshadowed by hydrodynamic contribution.

4.2.2 High-frequency range

The same approach is used for the high-frequency range considering a band-pass filter on the pressure field from 8000 Hz to 12000 Hz and reporting a generic time frame.

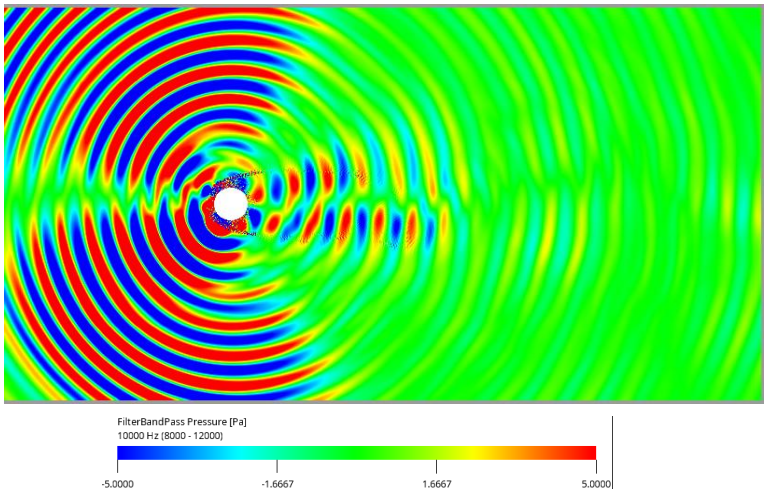

Figure 4.4 *Band-pass filter pressure 8000-12000 Hz*

As illustrated in the figure above, this approach yields improved results in terms of acoustic field visualization in the high-frequency range. In this specific range, where both formulations contribute comparably, the primary noise source comes from the cylinder itself. More specifically, it is associated with the coherent vortex shedding occurring around the small cylinders that constitute the structured porous medium that leads to the formation of the peak observed at St ≈ 12 in figure 4.1. The four preceding peaks are associated with vortex shedding from the small cylinders arranged in four distinct layers with different diameter, as described in the previous chapter.

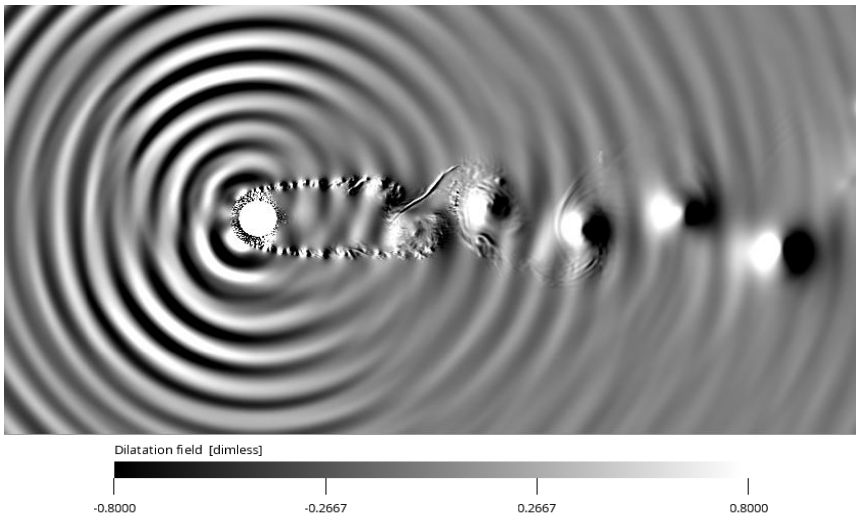

Figure 4.4 *Instantaneous dilatation field*

As observed in the dilatation field representation (i.e., the time derivative of the pressure field), the acoustic field is predominantly influenced by this high-frequency peak.

4.3 Crosswise pressure spectral decay

At this point in the analysis, in order to provide a physical interpretation of the previously presented results, the Power Spectrum of the pressure in the crosswise direction is examined across various frequencies. The curves below display the spectral decay at the streamwise position x = 6D and frequencies equal to St = 0.16, St = 0.4, St = 0.6 and St = 1.

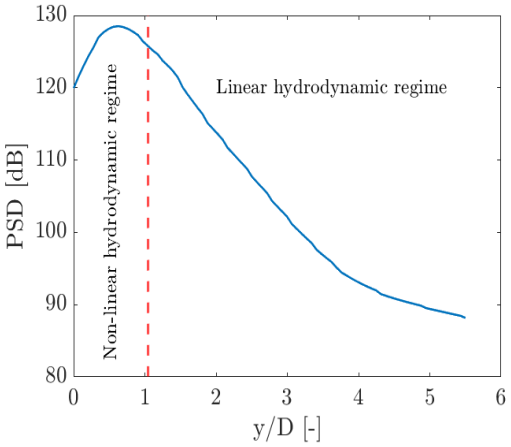

Figure 4.5 (a) *Spectral decay at St = 0.16*

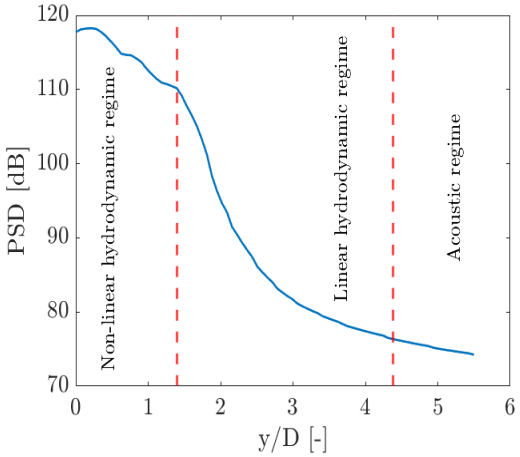

Figure 4.5 (b) *Spectral decay at St = 0.4*

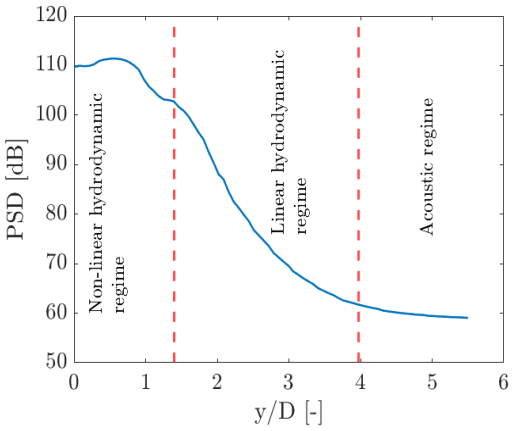

Figure 4.5 (c) *Spectral decay at St = 0.6*

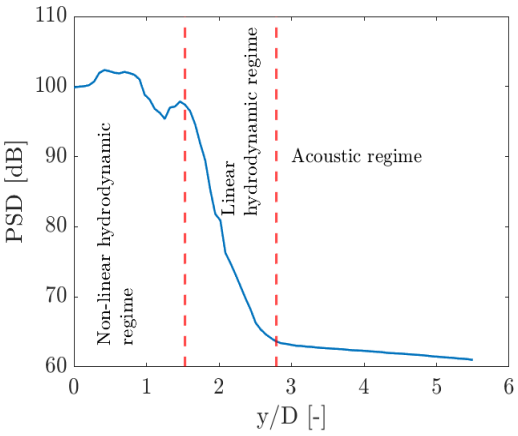

Figure 4.5 (d) *Spectral decay at St = 1*

It can be noted that three different zones can be identified: non-linear hydrodynamic regime, linear hydrodynamic regime and acoustic regime. The distribution that many authors (L.Rego et al. 2020, T. Suzuki and T. Colonius 2006) found for the jets have been retrieved. The non-linear hydrodynamic regime shows an irregular trend, while the linear hydrodynamic regime have an exponential decay along the crosswise direction, finally the acoustic regime displays a weaker exponential decay. From the figures presented above, it is evident that both the extent and location of the linear hydrodynamic regime are frequency-dependent. Specifically, higher frequencies exhibit a steeper spectral decay. Consequently, the transition to the acoustic regime, which has a weaker exponential decay, occurs at shorter distances compared to lower frequencies. This observation clarifies why, in the high-frequency range, the acoustic contribution can be detected even at relatively short distances when a band-pass filter approach is employed. This does not imply that the acoustic contribution is absent at shorter distances; rather, it is predominantly masked by the stronger hydrodynamic component.

Chapter 5 : Aerodynamic results

This section aims to offer a physical interpretation of the aeroacoustic findings discussed in the preceding chapter. Specifically, it focuses on identifying and analysing the most significant effects induced by the porous coating, along with their implications from an aeroacoustic standpoint. This chapter will be organised as follows: in the first part some aerodynamic quantities will be post-processed exploiting the commercial software PowerViz, while in the second part a different approach based on the computation of the coherence between near-field and far-field pressure and as well as between velocity fluctuations and far-field pressure will be presented in order to assess the relative weight of the scattered and direct acoustic sources on the far-field noise.

5.1 Velocity and vorticity plot

In the following figures (5.1 and 5.2) are plotted the instantaneous X-velocity and spanwise vorticity in dimensionless form based on the bare diameter and free-stream velocity.

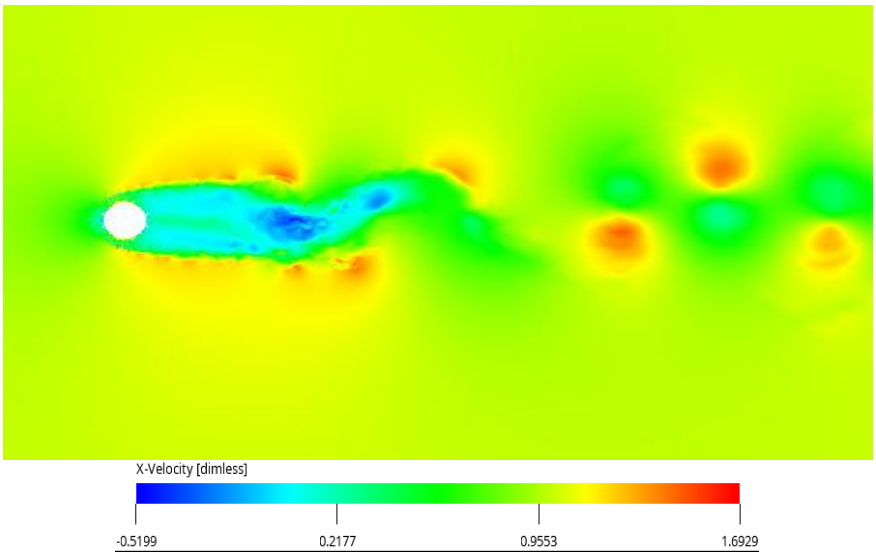

Figure 5.1 *Instantaneous X-velocity*

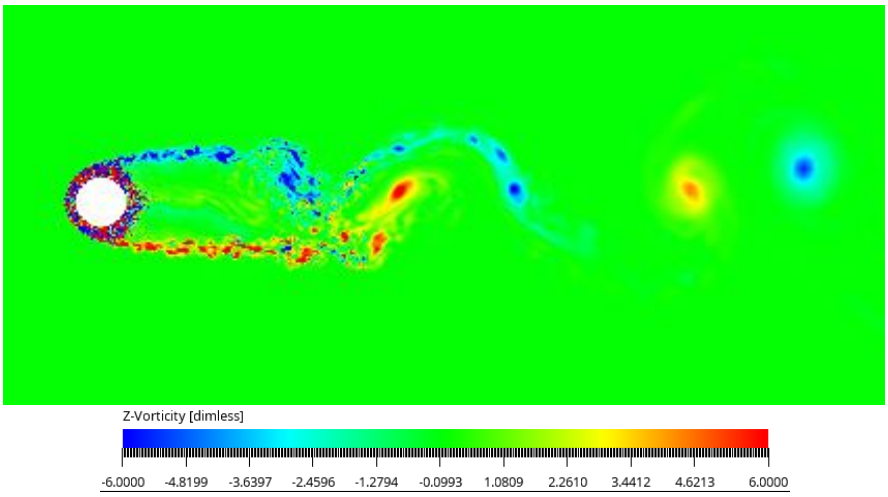

Figure 5.2 *Instantaneous spanwise vorticity*

From the figures above, a widening of the wake can be observed, with the shear layers starting to develop from the outermost diameter rather than the inner one, as would occur in the absence of the porous coating. Obviously this behaviour depends in the characteristics of the porous coating in terms of air-flow resistivity. From the Z-vorticity plot, it can be observed that the shear layers are initially thin and then begin to diverge near the recirculation zone. The distance over which this occurs is referred to as the vortex formation length. Moreover, the extreme values in the vorticity plot are manually set; otherwise, the peak values observed inside the porous medium would obscure the entire wake field. To analyse another relevant effect of the porous coating the time-averaged kinetic energy in dimensionless form is plotted.

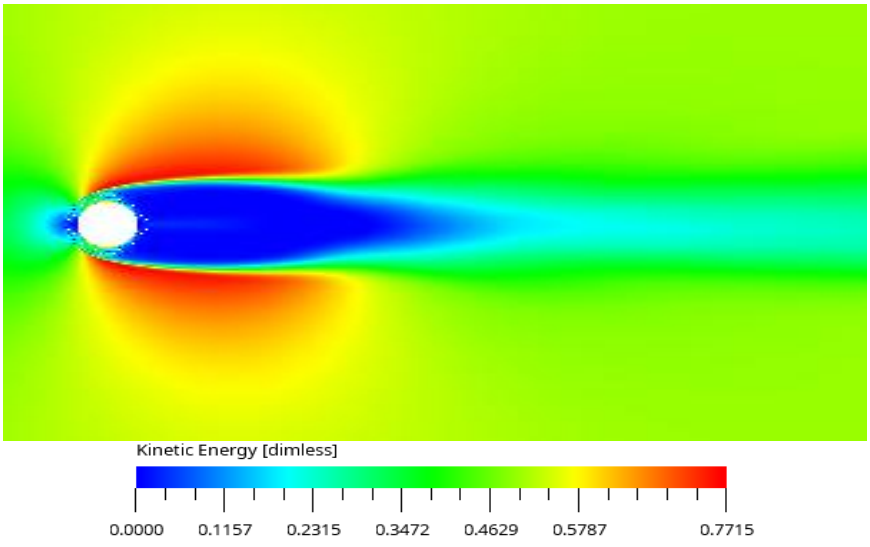

Figure 5.3 *Time-averaged kinetic energy*

From the figure 5.3, it can be seen that, as the flow penetrates the porous medium it undergoes energy attenuation due to the interaction with the small cylinders that constitute the porous medium. As a result, a constant injection of low energy flow downstream the cylinder takes place and a stable low-energy region is formed downstream the cylinder. This mechanism, together with the presence of slip velocity inside the porous medium, help to stabilize the shear layers and to shift both the recirculation zone and the position where the large scale vortices start to interact further downstream, leading to an increase of the vortex-formation length as well, that can be estimated in approximately 3.5÷4 diameters. In this case, the porous medium was specifically selected to maximise the extension of the vortex formation length, as this parameter is known to significantly reduce the efficiency of the scattering mechanism and the intensity of the resulting scattered source as well (Zamponi et al. 2024). In particular, when the vortex formation length is greater than 3.5 diameters the scattered contribution is deemed negligible, consistently with what has been just found in the previous chapter in the frequency range where the noise coming from the porous medium does not dominate (figure 4.1 and 4.2). Obviously, in a base configuration all there reasonings outlined above do not take place, as a consequence the roll-up of vortical structures starts close to the cylinder surface and the increasing in the vortex-formation length is not observed. To further investigate the wake pattern of the porous cylinder, the time-averaged x-velocity and y-velocity are plotted as a functions of y-positions at various x-positions.

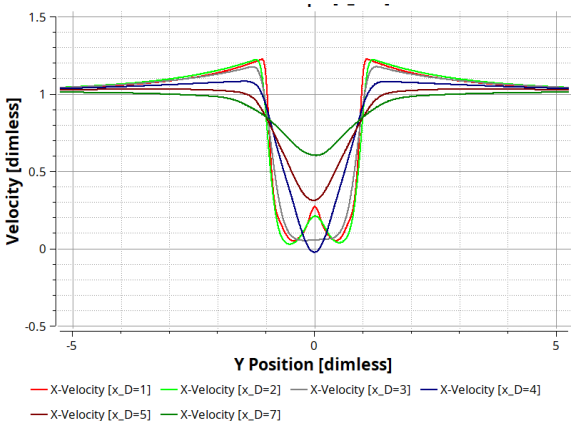

Figure 5.4 (a) *Time-averaged x-velocity at various x-stations*

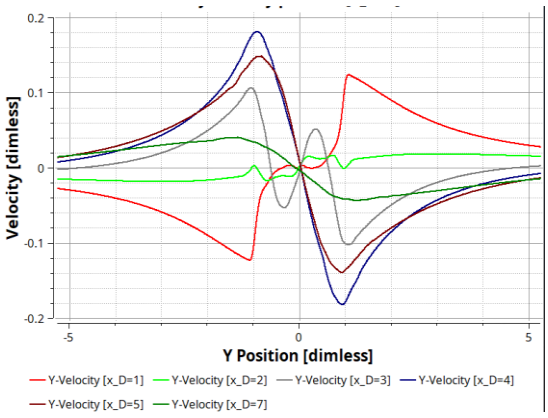

Figure 5.4 (b) *Time-averaged y-velocity at various x-stations*

Starting with the time-averaged x-velocity component, immediately downstream of the cylinder (at 1 and 2 diameters), two distinct minimum points can be observed, symmetrically positioned with respect to the y-axis. As a result, a local maximum appears along the y-axis. This phenomenon is likely related to the injection of the flow traveling through the innermost layer of the porous coating and the bare cylinder. The dissipation experienced by this portion of the flow is slightly lower compared to the rest of the flow that penetrates the porous medium. Moving further downstream the velocity profile tends to a "top-hat" profile with a constant minimum velocity, which is a sign of laminar flow ad low turbulence region. Finally a transition from such "top-hat" to a Gaussian-like profile with an unique minimum point takes place inside the recirculation zone. Moving further downstream the minimum point of the curve increases and the distance where the velocity joins the free-stream value increases as well. This is a clear indication that the wake widens as the x-distance increases. It can be demonstrated by plotting the wake width as a function of x (figure 5.5), where the width is defined as the distance from the y-axis at which the free-stream velocity is recovered.

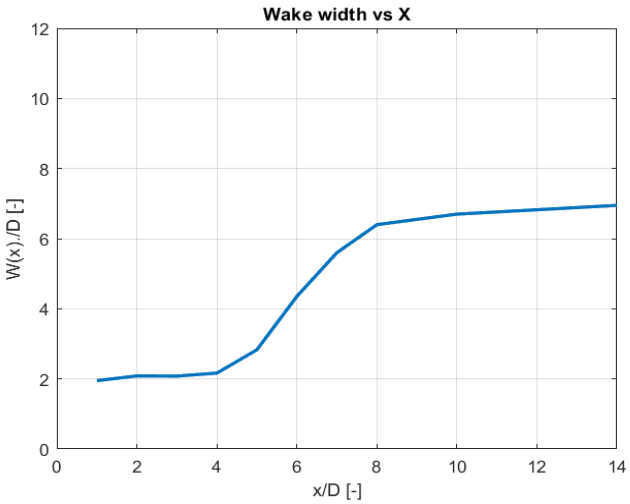

Figure 5.5 *Wake width vs x*

Regarding the y-component the maximum deficit respect to the zero value is observed in the recirculation zone, where two minimum point of opposite sign are disposed symmetrically respect to the y-axis due to the presence of two counterrotating recirculation bubbles (figure 5.6).

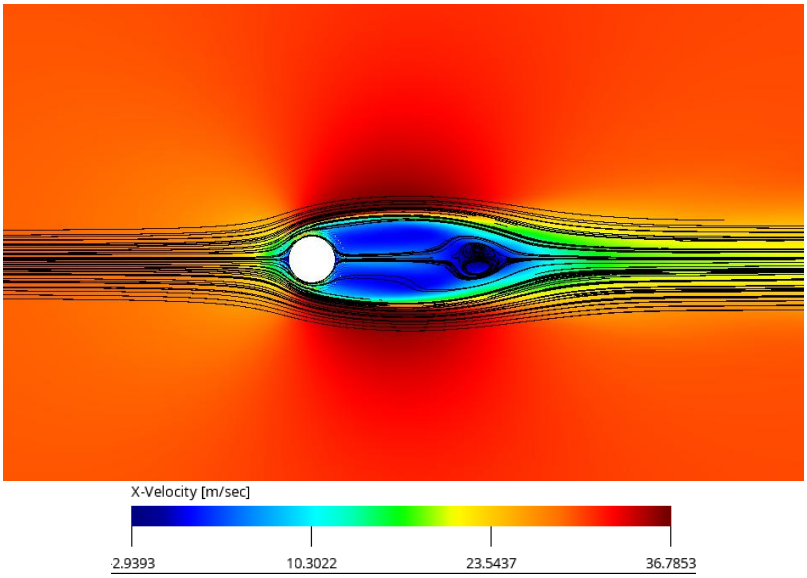

Figure 5.6 *Streamlines: focus on the recirculation zone*

In order to thoroughly analyse the vortex dynamic and convection the Q vortex identifier is computed, such physical quantity is used by PowerAcoustics to capture and detect the vortex in the flow field. It is obtained through the following formula:

$$Q = -0.5\left[\left(\frac{\partial u}{\partial x}\right)^2 + \left(\frac{\partial v}{\partial y}\right)^2 + \left(\frac{\partial w}{\partial z}\right)^2 + 2\frac{\partial u}{\partial y}\frac{\partial v}{\partial x} + 2\frac{\partial w}{\partial x}\frac{\partial u}{\partial z} + 2\frac{\partial v}{\partial z}\frac{\partial w}{\partial y}\right]$$

(5. 1)

Where u,v and w are x,y,z-components of velocity respectively. In the following figure, the Q-vortex identifier is plotted at the same instant of the x-velocity in figure 5.1 in dimensionless form.

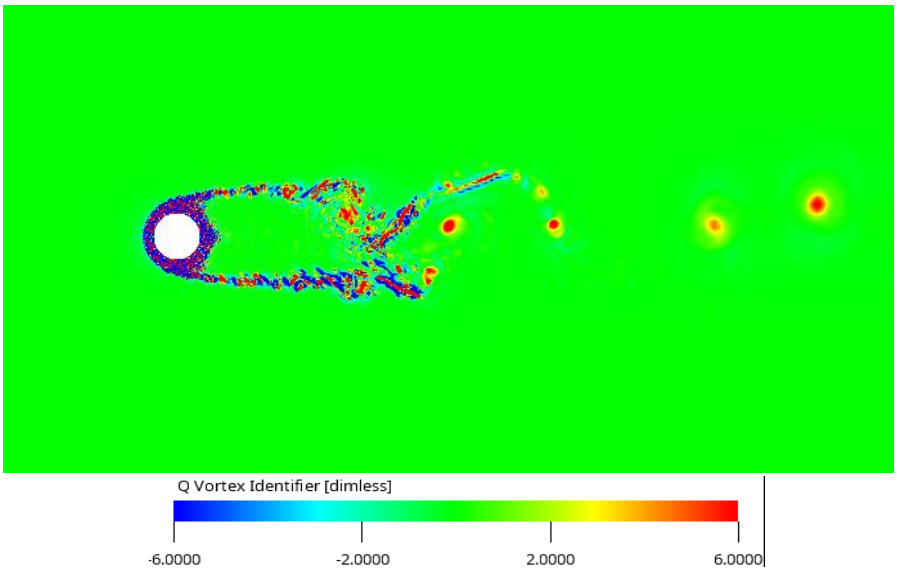

***Figure 5.7** Instantaneous Q vortex identifier*

With the figure above a better analysis of the vortex convection can be provided. At this time instant a vortical structure is detached from the upper shear layer and then it is carried away convectively by the mean flow. The Q-vortex identifier does not provide information on the direction of rotation; however, it can be inferred that vortices detaching from the upper shear layer rotate clockwise, while those originating from the lower shear layer rotate counterclockwise. Once these counterrotating vortices detached from the shear layer, they are submitted to a sudden acceleration and deformation, their interaction after the vortex-formation length is probably the cause of the quadrupolar source (i.e. direct acoustic source).

5.2 Reynolds stress distributions

Other important physical quantities useful to quantify the strength of the quadrupolar source are Reynolds stress, indeed, neglecting the viscous forces and assuming incompressible and isentropic flow, Lighthill's tensor can be expressed as $T_{ij} \approx \rho u_i u_j$. The Reynolds stress components in the xy-plane are reported in following figures, together with the turbulent kinetic energy (TKE), always in non-dimensional form $\left(\frac{\overline{u'u'}}{U_\infty^2}, \frac{\overline{v'v'}}{U_\infty^2}, \frac{\overline{u'v'}}{U_\infty^2}\right)$.

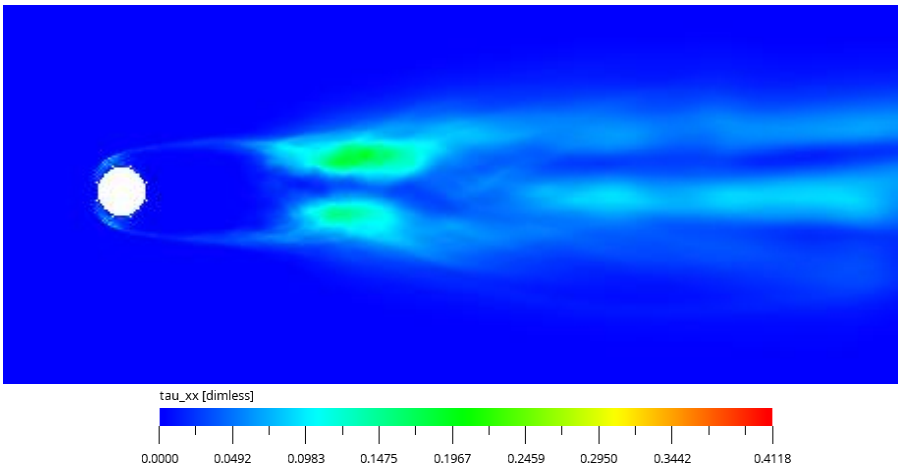

Figure 5.8 *Streamwise Reynolds stress*

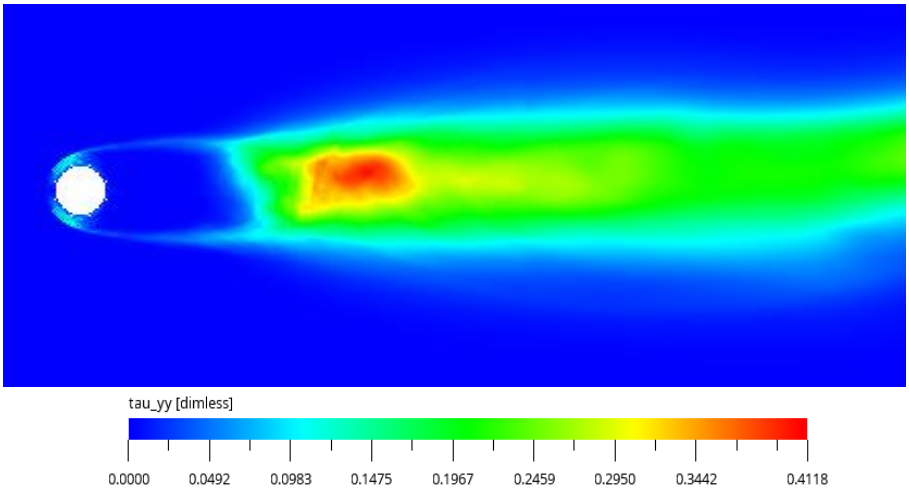

Figure 5.9 *Crosswise Reynolds stress*

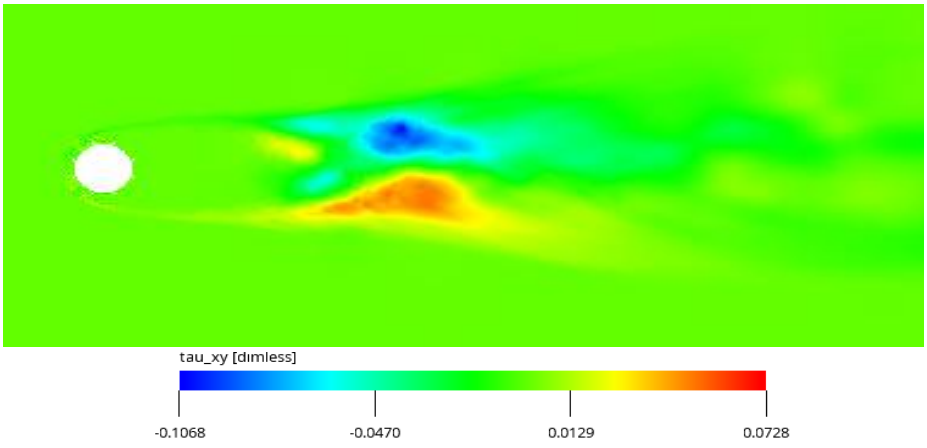

Figure 5.10 *Shear Reynolds stress*

Analysing the streamwise component, which is associated with flow recirculation, it attains two distinct maximum values corresponding to the two recirculation bubbles highlighted in Figure 5.6. However, it can be observed that the distribution is not entirely regular, as there are regions where the streamwise Reynolds stress value suddenly drops to zero without any physical justification. This is likely due to the limited physical time considered in the averaging process. Moreover, since these results are based on a partial simulation, the distribution lacks symmetry with respect to the x-axis. A more extended simulation is expected to yield a more symmetric distribution, where the two different maximum zones will become more clear and visible. Carrying on with crosswise component, since it is linked to the oscillatory movement of the turbulent structures, it has an unique maximum zone located where the eddies start to interact. Another relevant effect we can observe from the figure above is that the peak zones are spread on a relatively large area thanks to the widening of the wake mentioned before. Comparing the two components analysed above, it can be seen that the maximum of the crosswise component surpasses the maximum of the streamwise one by a factor two. This indicates that the large-scale vortices generated by vortex shedding predominantly oscillate in the vertical direction and they an important influence on the generation of vertical velocity fluctuations, which stand in as primary source of TKE. As consequence, from plot of the TKE (figure 5.11), we can see a distribution which is very close to that of crosswise component.

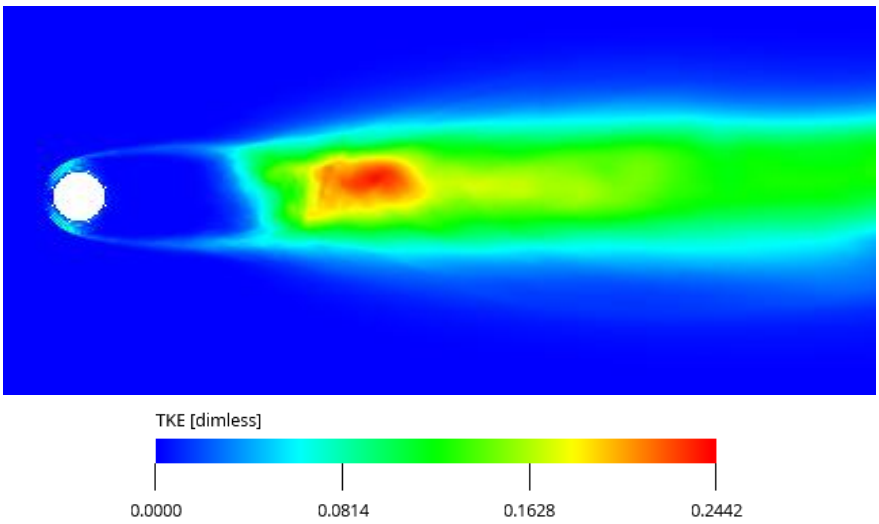

Figure 5.11 *Turbulent kinetic energy*

Large-scale vortices significantly contribute to the development of turbulence and turbulent kinetic energy (TKE), and these elements are key in the formation of quadrupolar sound sources. Their role can be also emphasized by plotting their instantaneous time derivative, computed with PowerAcoustics through the formula (A represents a generic quantity):

$$\frac{dA}{dt} = \frac{A(t_{j-2}) - 8A(t_{j-1}) + 8A(t_{j+1}) - A(t_{j+2})}{12\Delta t}$$

(5. 2)

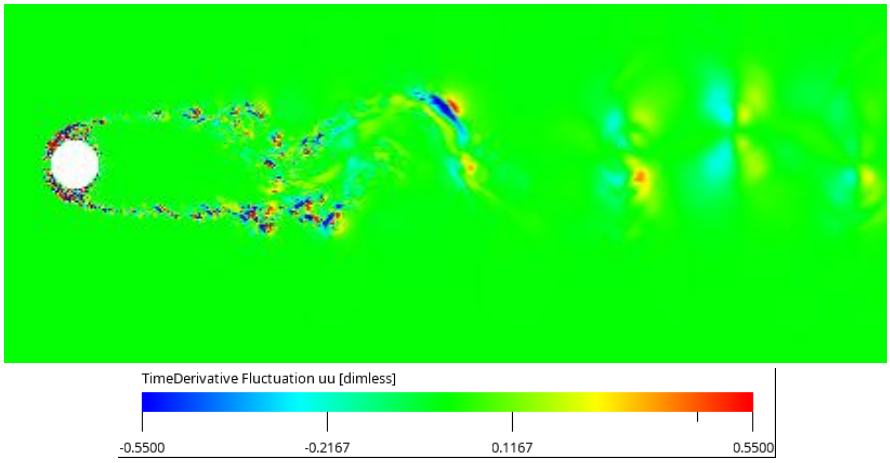

Figure 5.13 *Instantaneous Time derivative streamwise fluctuations*

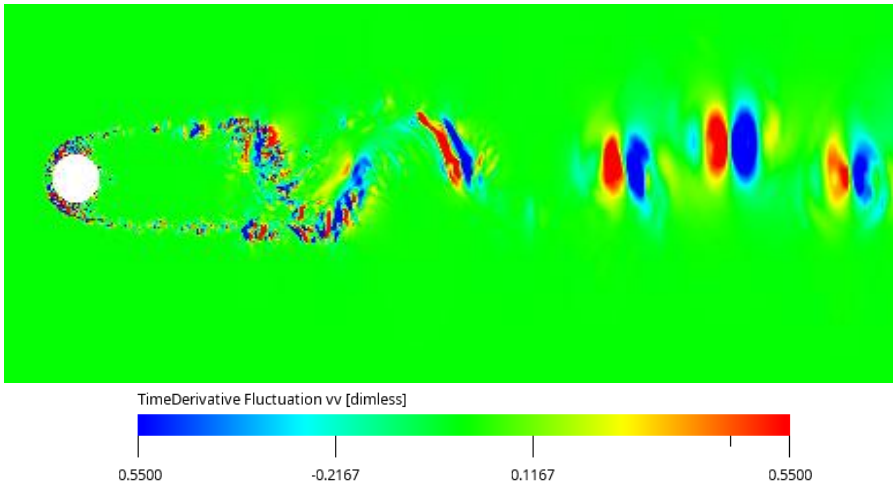

Figure 5.14 *Instantaneous Time derivative crosswise fluctuations*

The figures above illustrate that large-scale vortices and the onset of vortex shedding are areas where velocity fluctuations undergo the most rapid changes (excluding the region

within the porous medium). However, it should be noted that the extreme values in the legend are manually adjusted to improve visualization, as without this adjustment, the peak values within the porous medium would be obscured by the overall field. Nonetheless, in line with previous observations, the crosswise fluctuations exhibit more abrupt changes compared to their streamwise counterparts.

5.3 Coherence analysis

In the second part of this chapter, the relative contributions of quadrupolar and dipolar sources are evaluated by computing the coherence between far-field pressure and velocity fluctuations, as well as between far-field pressure and surface pressure fluctuations. These calculations are carried out following the formulation introduced in Chapter 2. Focusing first on the former, the following two figures report the coherence at the shedding frequency in the form of contour plot considering both velocity components in the x-y plane. For the far-field pressure a microphone placed at (0, 1, 0) [m] is considered.

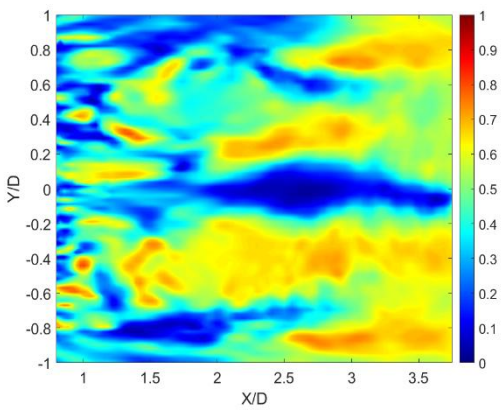

Figure 5.15 (a)

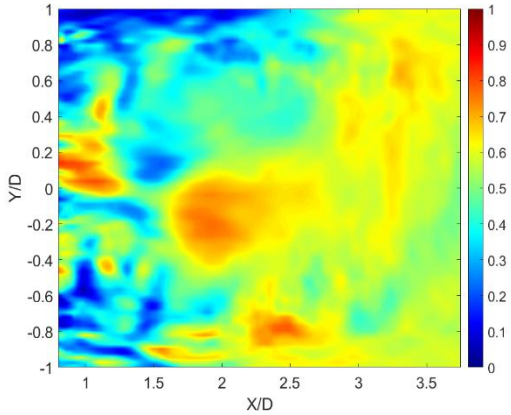

Figure 5.15 (b)

Fig 5.15 *Coherence at the shedding frequency between far field pressure (microphone position (0, 1, 0) [m]) and streamwise (a) and crosswise (b) velocity fluctuations*

For the far-field pressure the FWH permeable formulation has been employed, thereby enabling a direct comparison between the relative contributions of the two source types. From figures above, it can be noted that the peak values of coherence between far-field pressure and streamwise velocity fluctuations follow the shear layers trajectories, becoming zero at y/D = 0. In contrast, when the coherence is computed using the crosswise component, the peak values appear to be distributed across all the measurement

points, where the time-history of velocity fluctuations have been evaluated. These findings provide insights about the role of the velocity field to the direct propagation of acoustic waves as a quadrupole. To allow for a direct comparison with the dipolar source, the coherence between far-field and near-field pressure fluctuations has been evaluated, as the latter are directly involved in the scattering mechanisms. For this purpose, specific points on the cylinder surface and within the wake region have been selected to extract the time histories of near-field pressure and velocity fields, respectively.

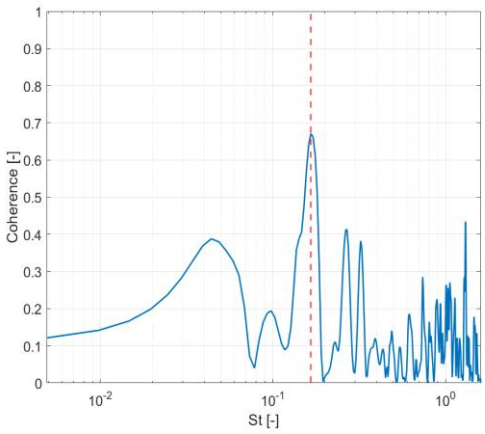

Figure 5.16 (a)

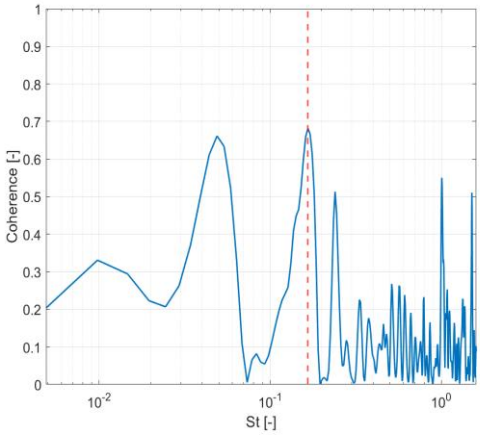

Figure 5.16 (b)

Figure 5.16 *Coherence between streamwise (a) and crosswise (b)velocity fluctuations at (x, y, z) = (4D, 0.5 D_{ext}, 0) and far-field pressure with microphone position (0,1,0) [m] based on FWH permeable formulation*

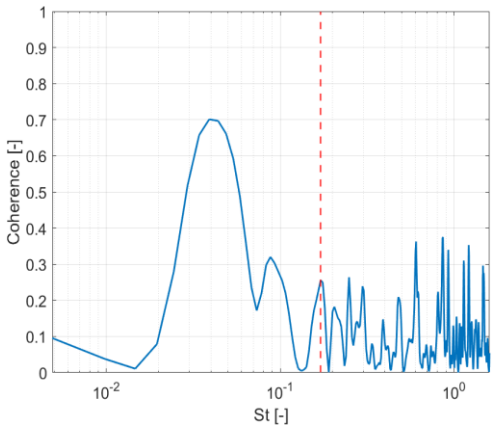

Figure 5.17 (a)

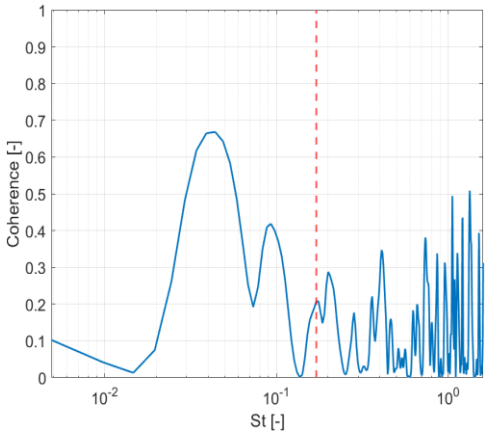

Figure 5.17 (b)

Figure 5.17 *Coherence near-field pressure fluctuations at $\theta = 50°$ (a) and $\theta = 90°$ (b) and far-field pressure with microphone position at (0, 1, 0) [m] based on FWH permeable formulation (i.e. angles are defined in a way that $\theta = 180°$ is on the stagnation line)*

From figures above, it can easily be noted that at the shedding frequency, which is marked with red dotted line, the coherence between both velocity fluctuations and far field pressure ($\gamma^2_{p,p_s}(f_{Sh}) < \gamma^2_{p,u}(f_{Sh})$ and $\gamma^2_{p,p_s}(f_{Sh}) < \gamma^2_{p,v}(f_{Sh})$). To gain a more comprehensive understanding of the analysis, additional points have been considered both in the wake region and on the cylinder surface.

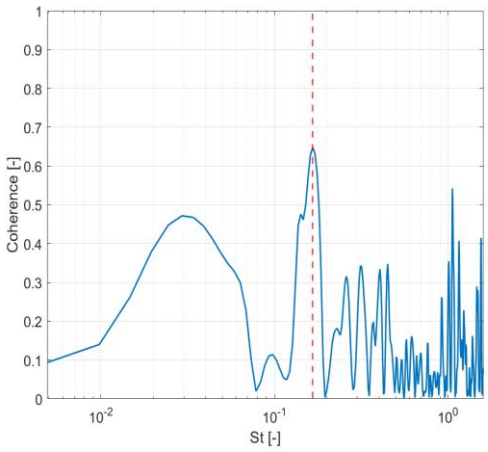

Figure 5.18 (a)

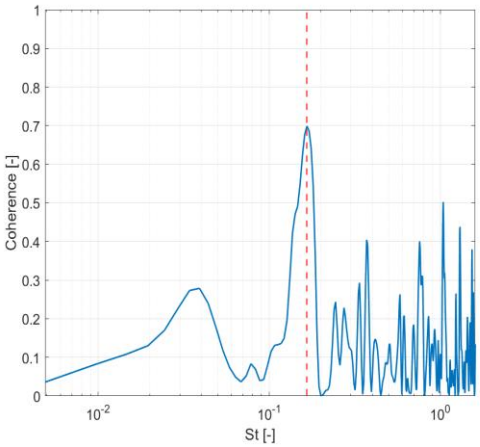

Figure 5.18 (b)

Figure 5.18 *Coherence between streamwise (a) and crosswise (b)velocity fluctuations at (x, y, z) = (4.5D, 0.5 D_{ext}, 0) and far-field pressure with microphone position (0,1,0) [m] based on FWH permeable formulation*

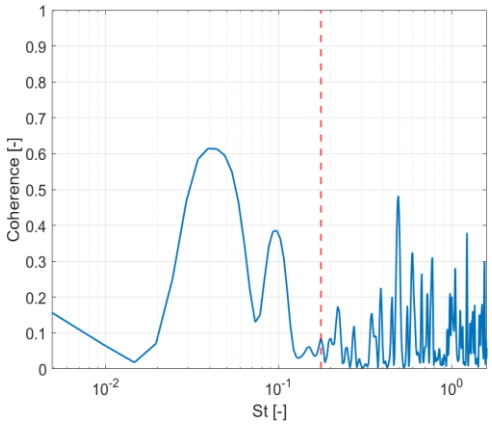

Figure 5.19 (a)

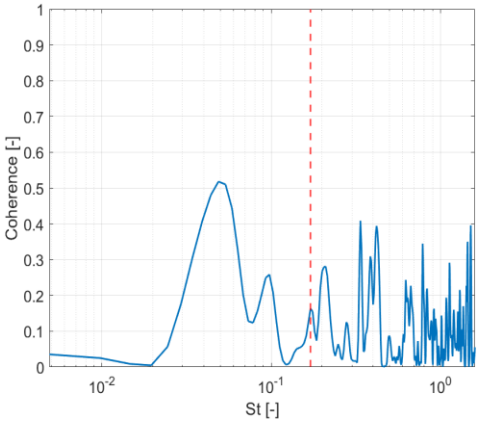

Figure 5.19 (b)

Figure 5.19 *Coherence near-field pressure fluctuations at $\theta = 130°$ (a) and $\theta = 180°$ (b) and far-field pressure with microphone position at (0, 1, 0) [m] based on FWH permeable formulation*

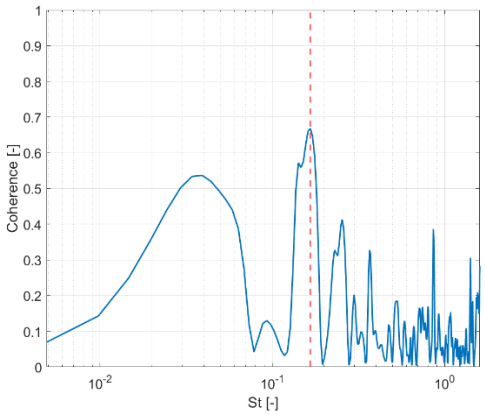

Figure 5.20 (a)

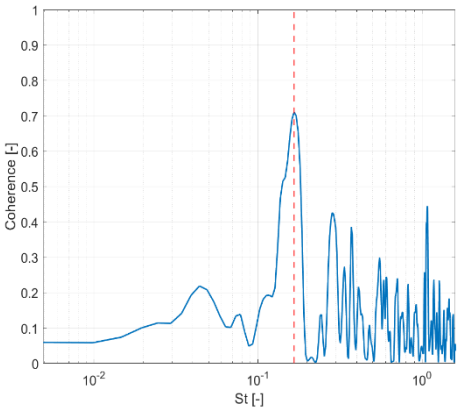

Figure 5.20 (b)

Figure 5.20 *Coherence between streamwise (a) and crosswise (b) velocity fluctuations at (x, y, z) = (5D, 0.5 D_{ext}, 0) and far-field pressure with microphone position (0,1,0) [m] based on FWH permeable formulation*

Even when additional points are considered, the previously observed trend is consistently recovered ($\gamma^2_{p,p_s}(f_{Sh}) < \gamma^2_{p,u}(f_{Sh})$ and $\gamma^2_{p,p_s}(f_{Sh}) < \gamma^2_{p,v}(f_{Sh})$). As a result it is confirmed that the direct acoustic source has a greater impact than that provided by the scattered one. However it must be kept in mind that this analysis provides insights into the relative contributions of the two sources, rather than their absolute contributions. Another noteworthy observation from the figures above is that the peak coherence between far-field pressure and crosswise velocity fluctuations ($\gamma^2_{p,v}(f_{Sh})$) is slightly higher than that obtained with the streamwise component ($\gamma^2_{p,u}(f_{Sh})$). This indicates that vertical velocity fluctuations have a greater influence on the far-field noise compared to their streamwise counterparts, reaffirming their critical role as highlighted in the previous section. All the aforementioned analyses have been carried out using far-field data obtained through the FWH permeable formulation, which accounts for both dipolar and quadrupolar sources. To complete this section, the same analyses have also been conducted using far-field data derived from the FWH solid formulation.

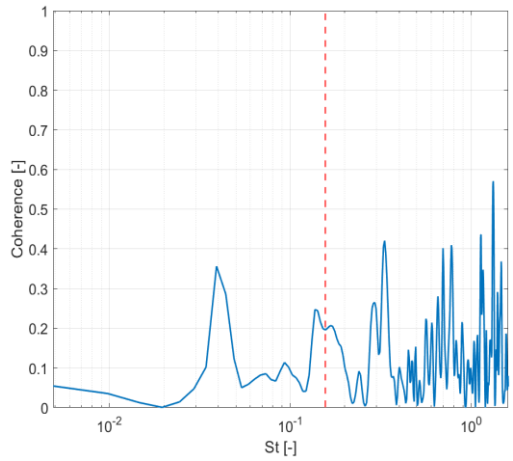

Figure 5.21 (a)

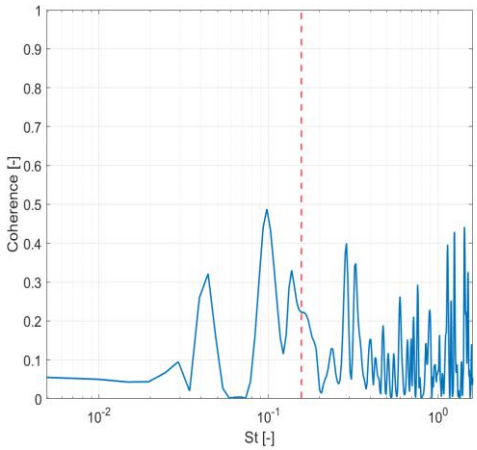

Figure 5.21 (b)

Figure 5.21 *Coherence between streamwise (a) and crosswise (b)velocity fluctuations at (x, y, z) = (4D, 0.5 D_{ext}, 0) and far-field pressure with microphone position (0,1,0) [m] based on FWH solid formulation*

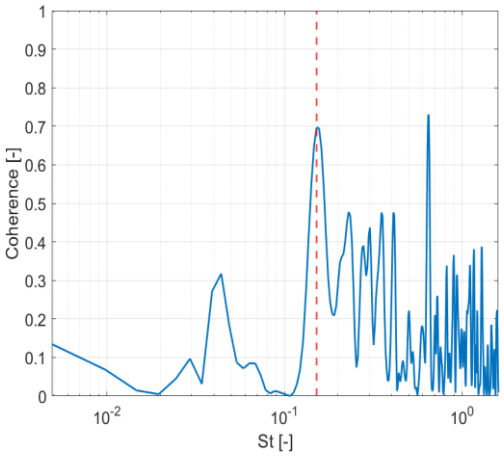

Figure 5.22 (a)

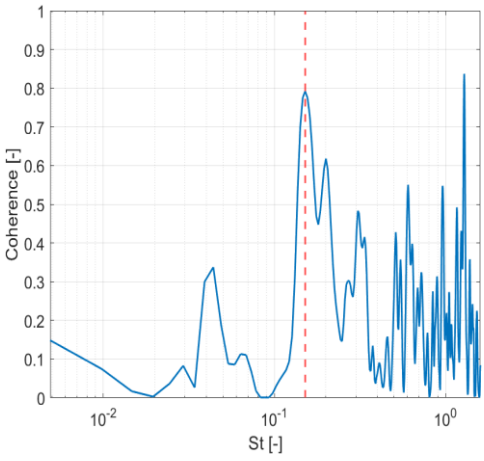

Figure 5.22 (b)

Figure 5.22 *Coherence near-field pressure fluctuations at $\theta = 50°$ (a) and $\theta = 90°$ (b) and far-field pressure with microphone position at (0, 1, 0) [m] based on FWH solid formulation (i.e. angles are defined in a way that $\theta = 180°$ is on the stagnation line)*

In contrast to the results presented in Figures 5.16 through 5.20, the data shown in Figures 5.21 and 5.22 reveal an opposite trend, indeed it can be noted that $\gamma^2_{p,p_s}(f_{Sh}) > \gamma^2_{p,u}(f_{Sh})$ and $\gamma^2_{p,p_s}(f_{Sh}) > \gamma^2_{p,v}(f_{Sh})$. Nevertheless, these results are not in contradiction with the previous findings, as it is important to recall that the FWH solid formulation accounts

solely for the dipolar source. Given that this source is associated with pressure fluctuations on the cylinder surface, the presence of a peak at the shedding frequency in the coherence plots between far-field and near-field pressure is consistent with expectations.

Chapter 6: Near-field pressure analysis

This chapter aims to conduct an in-depth analysis of the near-field pressure spectra surrounding the cylinder surface, with a particular focus on identifying the dominant frequencies present, investigating their potential underlying causes. A coherence analysis between velocity fluctuations and near-field pressure will be performed to evaluate the role of vortex shedding in imposing surface pressure fluctuations.

6.1 Near-field pressure PSD

The near-field pressure PSD is depicted in the following figure, considering the time histories in 45 points equally spaced around the solid cylinder ranging from 180° to 0°.

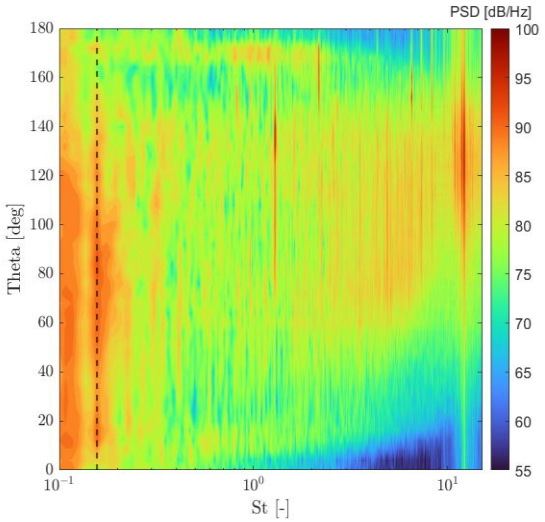

Figure 6.1 *Near-field pressure PSD around the bare cylinder. The black dotted line represents the shedding frequency*

From above figure there is a clear evidence of a contribution at the shedding frequency, that is highlighted with the black dotted line in the figure, which is maximum away from the stagnation points and tends to decrease especially while moving towards the rear stagnation point (θ = 180°). To further enrich the analysis, PSD is examined at specific angles from those considered in the figure above (θ = 0°, 40°, 90°, 120°, 180°).

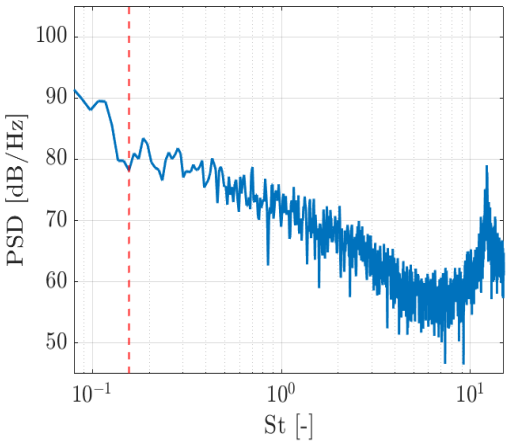

Figure 6.2 (a)

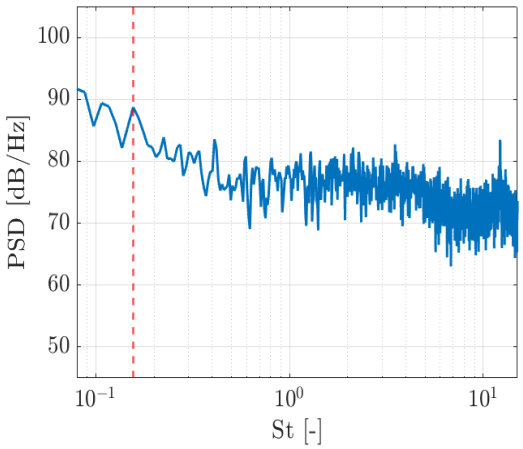

Figure 6.2 (b)

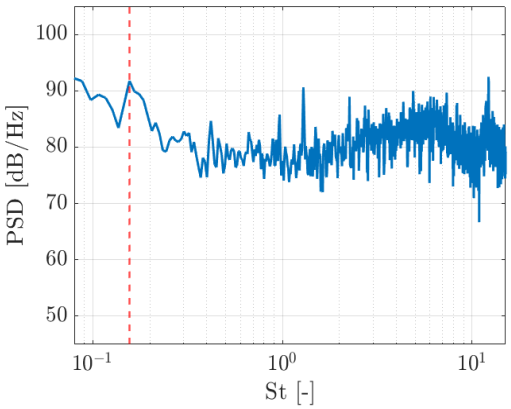

Figure 6.2 (c)

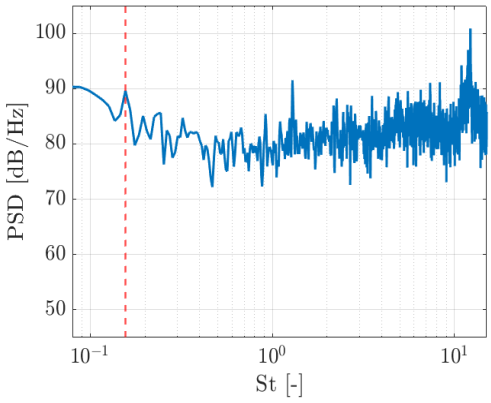

Figure 6.2 (d)

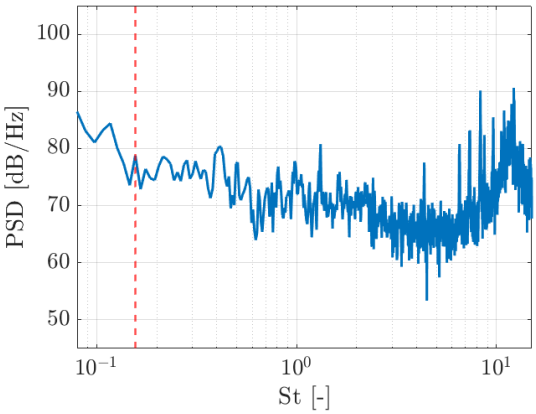

Figure 6.2 (e)

Figure 6.2 *Near-field pressure spectra at $\theta = 0°$ (a), 40°(b), 90°(c), 120°(d) and 180° (e). The red dotted lines represent the shedding frequency*

Consistently with what it has been observed previously, for curves corresponding to angles far from both the front and rear stagnation points (i.e., at θ = 0° and θ = 180°, respectively), a distinct peak emerges at the shedding frequency. By contrast for the two curved corresponding to the stagnation points such peak is suppressed. These observation suggests a strong correlation between vortex shedding and surface pressure fluctuations, which have a primary role in scattering acoustic waves. Moreover, a greater broadband content is observed at θ = 90°, 120°, and 180°, compared to the other angles considered. This can be explained by noting that the high-frequency contribution -briefly analysed in Chapter 4- exhibits its maximum directivity in the windward region. This explains the presence of a more pronounced high-frequency peak at these angles. To further investigate the effect of vortex shedding on the surface, the near-field pressure at the shedding frequency is presented considering all angles around the surface.

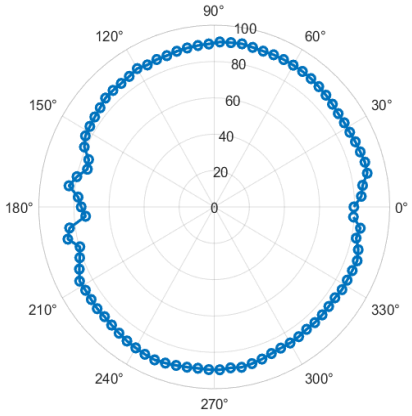

Figure 6.2 *PSD near-field pressure at the shedding frequency*

From above figure, it can be confirmed that the PSD at the shedding frequency gradually increases moving from the stagnation point, reaching its peak value (92 dB) at θ ≈ 80°, and then it decreases again moving towards θ = 0° reaching a value of 78 dB. Same results can be retrieved also considering angles corresponding to negative y-coordinates. The stagnation points are also the zones that are less influential in scattering the acoustic waves to the far-field, as it can be seen in figure 6.4, where the coherence between the surface pressure and far-field pressure based on FWH solid formulation is reported. This result confirms the dipolar directivity of the scattered acoustic source. Nevertheless, it can be deduced that there is an upstream influence of the vortex shedding, likely through

a feedback loop as hypothesized by some authors (Maryami, Reza and Liu, Yu (2024)), that induces surface pressure fluctuations.

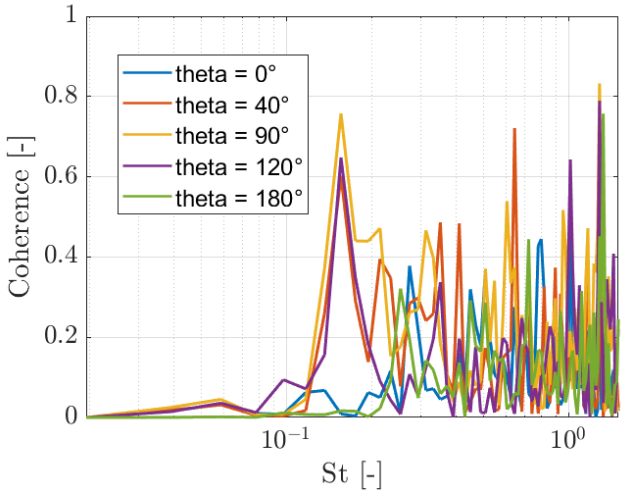

Figure 6.3 *Coherence between near-field pressure and far-field pressure based on FWH solid formulation considering a microphone placed at θ=90° with a distance of 1 m from cylinder*

6.2 Velocity fluctuations – near-field pressure coherence

In the previous section, it was demonstrated that vortex shedding exerts an upstream influence, generating pressure fluctuations on the surface of the cylinder. To further investigate the mechanisms by which these pressure disturbances are transmitted, the coherence between both components of velocity fluctuations in the wake and near-field surface pressure will be evaluated, considering a grid of points downstream the cylinder and isolated points at different angles on the surface in both leeward and windward regions, respectively.

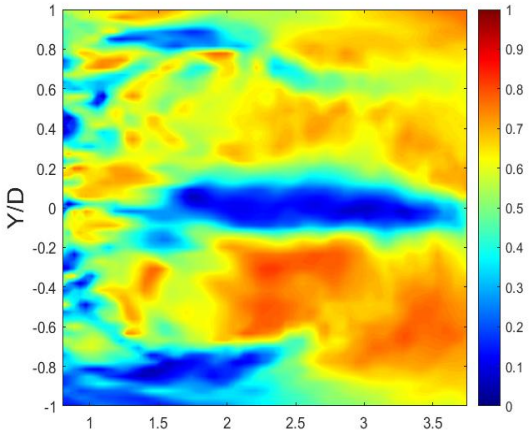

Figure 6.4 (a)

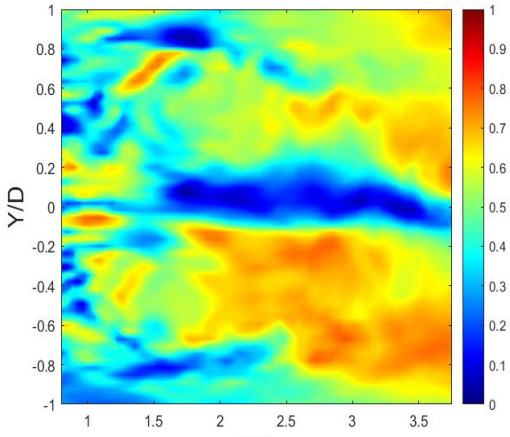

Figure 6.4 (b)

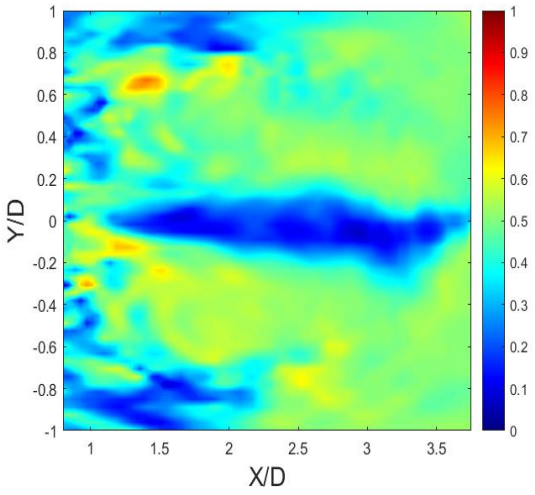

Figure 6.4 (c)

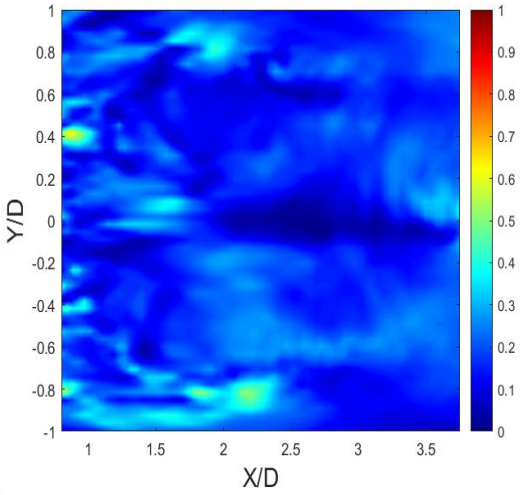

Figure 6.4 (d)

Figure 6.4 *Coherence at the shedding frequency between streamwise velocity fluctuations and near-field pressure at 50° (a), 90° (b), 130° (c), 180° (d)*

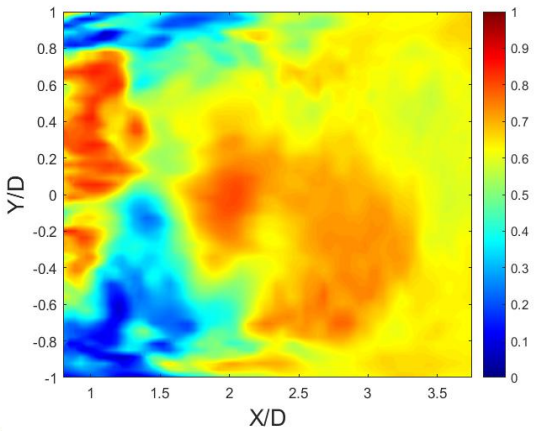

Figure 6.5 (a)

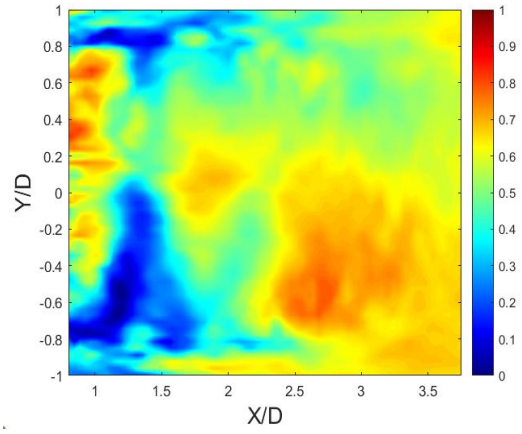

Figure 6.5 (b)

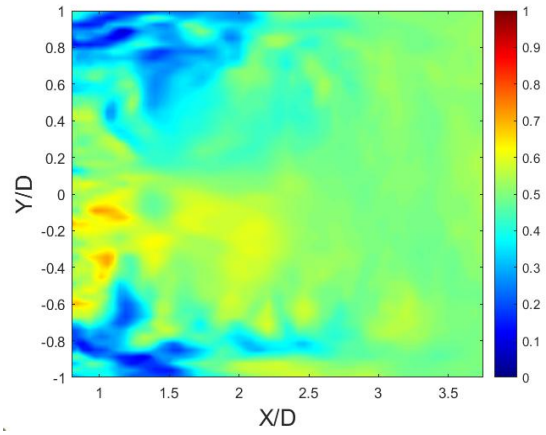

Figure 6.5 (c)

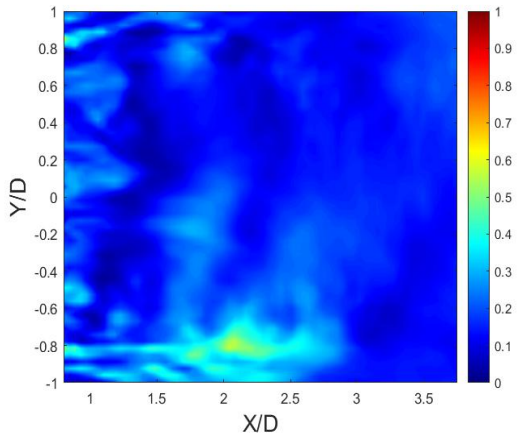

Figure 6.5 (d)

Figure 6.5 *Coherence at the shedding frequency between crosswise velocity fluctuations and near-field pressure at 50° (a), 90° (b), 130° (c), 180° (d)*

From figures above, it is evident that, for both components, the resulting distributions closely resemble those associated with the coherence between far-field pressure and velocity fluctuations presented in the previous chapter. This inform us that velocity fluctuations, at the shedding frequency, are directly involved in imposing both near-field, through a feedback signal, and far-field pressure. Consistently, the peak coherence values for streamwise velocity fluctuations are observed along the trajectory of the shear layers. In contrast, those associated with crosswise velocity fluctuations appear to be more uniformly distributed across all measurement points. Another noteworthy trend observable in the figure above is the gradual decrease in overall peak coherence values for both components as one moves from the leeward to the windward region. This behaviour may be attributed to the fact that any potential signal originating from the wake—such as a feedback mechanism—must travel a longer distance to reach the windward side, thereby experiencing attenuation along its path. This analysis reveals the influence of velocity fluctuations on imposing near-field pressure fluctuations at the shedding frequency, however the precise mechanism through which this influence appears remains unclear. A further investigation about the eventual presence of a feedback contribution will be provided in the following chapter post-processing SPOD results.

6.2.1 Coherence analysis on porous coating

In the second part of this section, the coherence between velocity fluctuations and near-field pressure was computed for each layer of the porous medium. Specifically, for one of the four porous layers, the coherence between velocity fluctuations - sampled at a point in the wake - and the near-field pressure - sampled on each small cylinder within the selected porous layer - was evaluated. The pressure sampling point on each cylinder was not chosen arbitrarily; rather, it was selected as the location where the maximum root mean square (RMS) pressure value was observed. This search was limited to the leeward side of each small cylinder, as this region is most likely to be affected by potential feedback contributions from the wake. Including the windward region would have biased the analysis, since the maximum RMS pressure would consistently be found there due to the influence of the wake from the upstream cylinder.

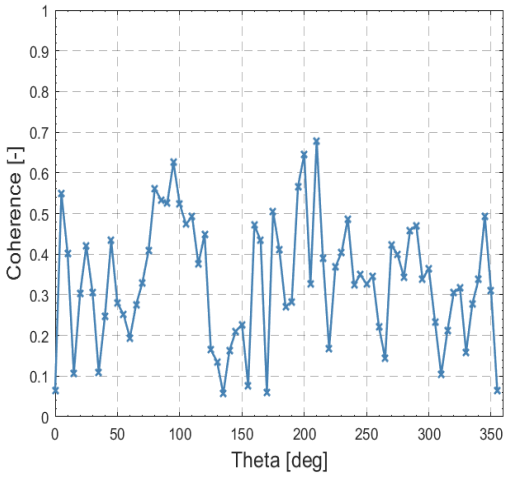

Figure 6.6 (a)

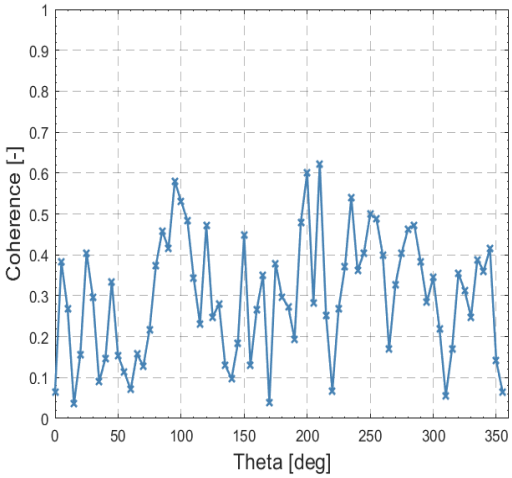

Figure 6.6 (b)

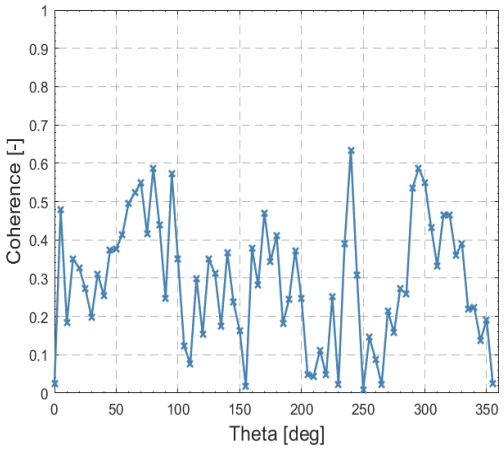

Figure 6.6 (c)

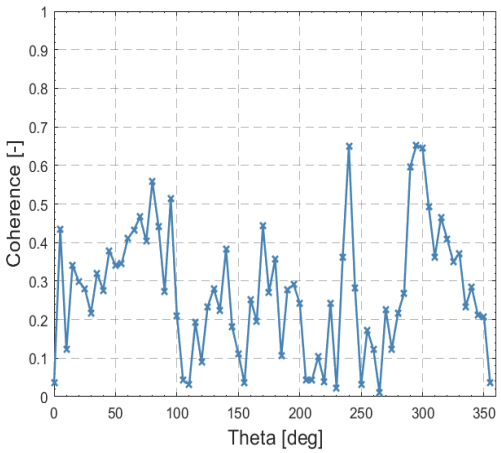

Figure 6.6 (d)

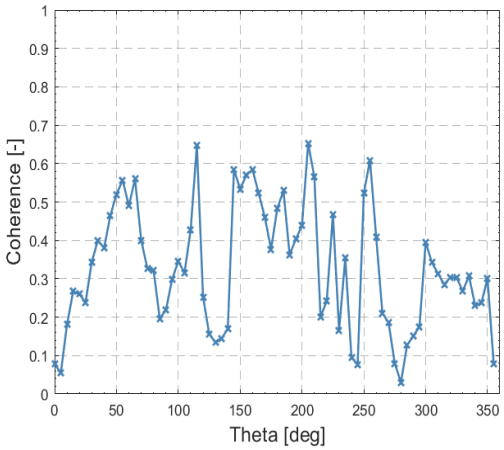

Figure 6.6 (e)

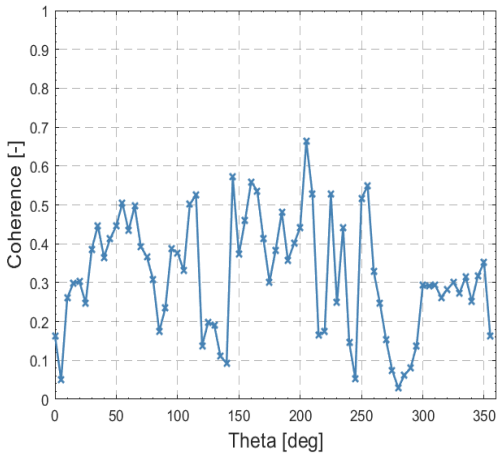

Figure 6.6 (f)

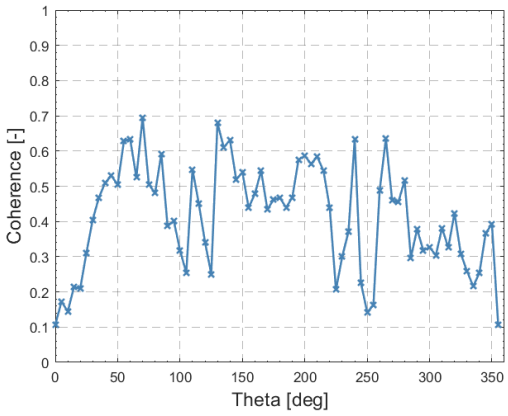

Figure 6.6 (g)

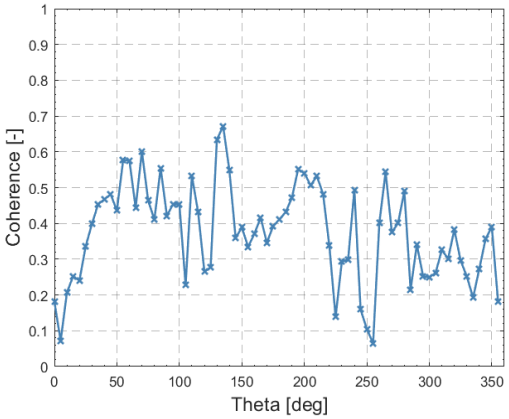

Figure 6.6 (h)

Figure 6.6 *Coherence at the shedding frequency between streamwise (a, c, e, g) and crosswise (b, d, f, h) velocity fluctuations at (3.5D, 0.5$D_{ext,0}$) and near-field pressure in the point of maximum RMS in the leeward region of the each cylinder of layer 1 (innermost) (a, b), layer 2 (c, d), layer 3 (e, f), layer 4 (outermost) (g, h)*

In the above figures are reported the results of the calculation previously explained, in particular they report the coherence at the shedding frequency as a function of the angular position of each small cylinder of each porous layer. It can be seen that the separation points at $\theta = 110° \div 120°$ and $\theta = 250° \div 260°$ coincide with a decrease of the coherence values for all porous layers. Relatively low values of coherence are observed at $\theta = 0°$ and 180° as well. What is a little strange is the lack of symmetry of the coherence values between angles at negative and positive y-semiaxes, this could be due to the choice of the point where velocity fluctuations are sampled, even small variations of such could take better results. Following the reasoning proposed in the last section regarding the weakening of a feedback signal with the distance, another trend that could be observed is a decreasing of the coherence values in the windward region compared to those in the leeward one. This trend is observable only for the 2^{nd} innermost layer (figures 6.6 (c) and (d)).

Chapter 7: Spectral Proper Orthogonal Decomposition

In this chapter Spectral Proper Orthogonal Decomposition (SPOD) is applied to analyse the wake of a cylinder. A brief theoretical background on SPOD and its underlying algorithm ,along with a justification for the selection of spectral parameters used in this study is presented in the second chapter. In the first section of the present chapter, a convergence analysis is carried out by progressively increasing the number of spatial sampling points in both the crosswise and streamwise directions. The resulting SPOD modes are then discussed, and a comparison is made with a reference case in which the solid cylinder is included within the computational domain. Finally, the SPOD modes are post-processed to investigate the possible presence of a feedback mechanism. A hypothesis regarding the feedback loop is formulated, along with a physical interpretation of the noise mitigation effects associated with the porous coating.

7.1 Convergence analysis

This section aims to assess the independence of the selected point grid used in the SPOD analysis. Specifically, the number of points in both the streamwise and crosswise directions is progressively increased until negligible variations are observed in the mode amplitudes at certain frequencies. The convergence analysis will focus on low-order modes at low frequencies since, as we will see in the next section, they carry a more significant energy contribution.

7.1.1 Streamwise convergence analysis

The number of points in the streamwise direction, N_X, is gradually increased from 260 to 400. Convergence is assessed by plotting the first two modes at the shedding frequency, as well as at its odd and even harmonics.

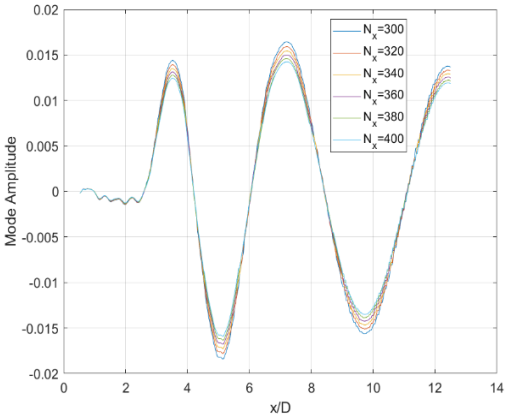

Figure 7.1 (a)

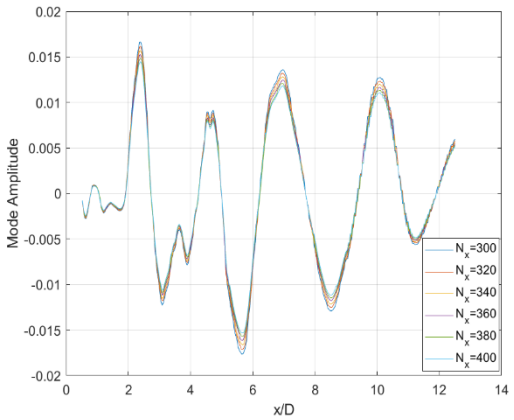

Figure 7.1 (b)

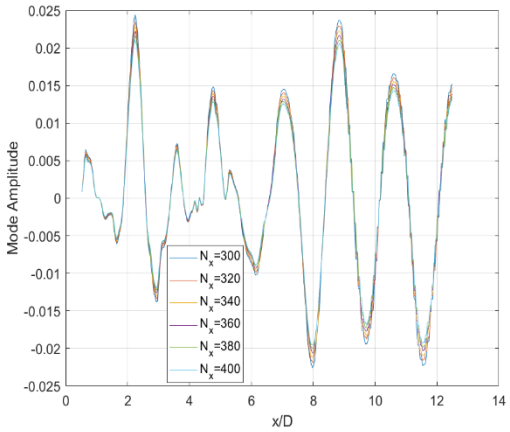

Figure 7.1 (c)

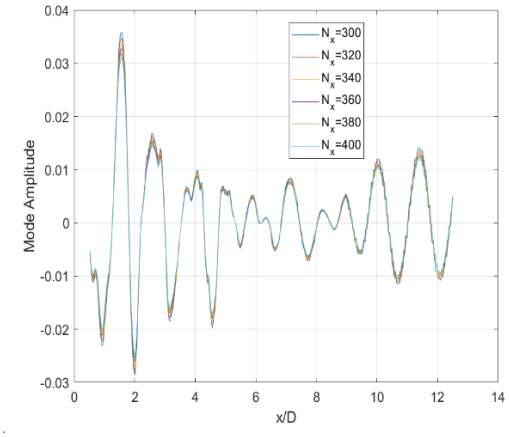

Figure 7.1 (d)

***Figure** 7.1 Convergence analysis amplitude mode 1at y/D=1 at the shedding frequency f_{SH} (a), $2f_{SH}$ (b), $3f_{SH}$ (c), $4f_{SH}$ (d)*

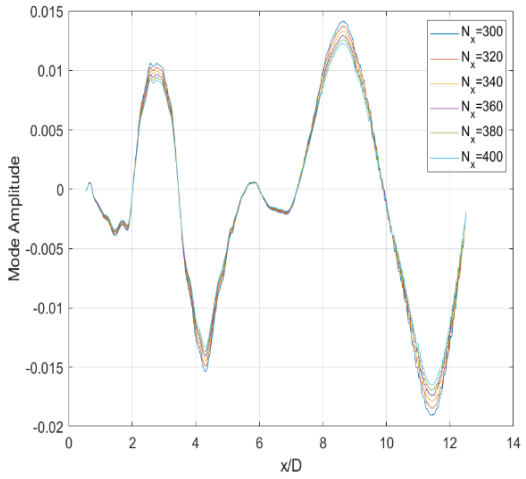

Figure 7.2 (a)

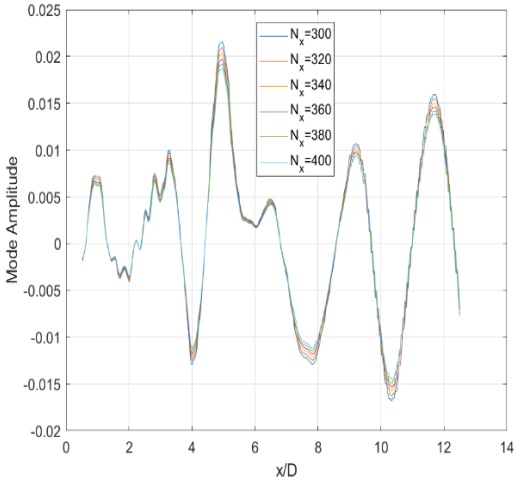

Figure 7.2 (b)

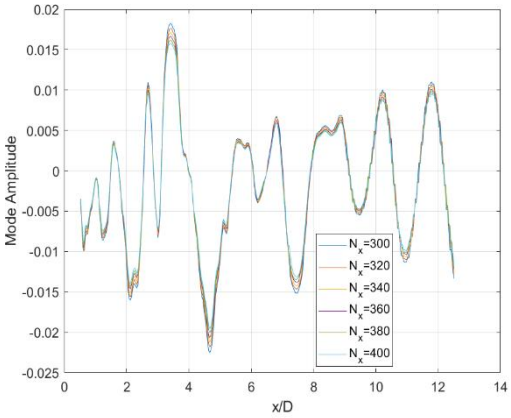

Figure 7.2 (c)

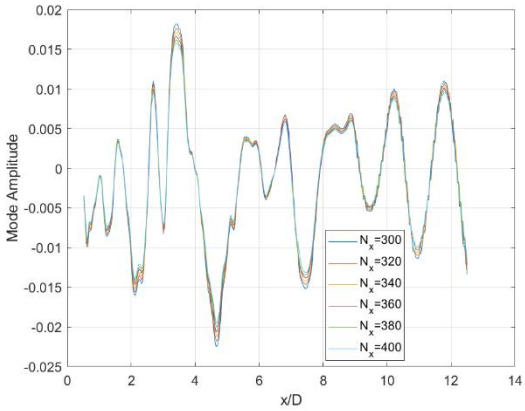

Figure 7.2 (d)

Figure 7.2 *Convergence analysis amplitude mode 2 at y/D=1 at the shedding frequency f_{SH} (a), $2f_{SH}$ (b), $3f_{SH}$ (c), $4f_{SH}$ (d)*

It can be observed that convergence is satisfactory for all the analysed frequencies in both modes. Taking into account the first mode at the shedding frequency (figure 7.1 (a)), a discrepancy of about 3% between the last two curves (N_X = 380 and N_X = 400) is observed. Same trend is observable for the other frequencies in both modes. However, if also mid-high frequencies are taken into account the convergence will be not as satisfactory, since small structures are involved and a better spatial resolution and computational cost is needed, moreover they carry a negligible amount energy compared

to the low frequencies. Considering a trade-off between a good spatial resolution and computational cost a number of points equal to 380 is selected.

7.1.2 Crosswise convergence analysis

A similar analysis have been conducted increasing the number of points along the crosswise direction. As before convergence is assessed plotting the first two modes at the shedding frequency and its first two even and odd harmonics.

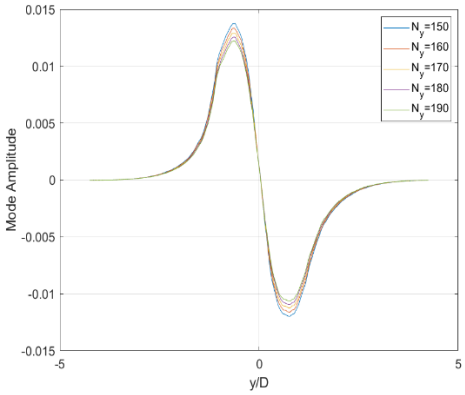

Figure 7.3 (a)

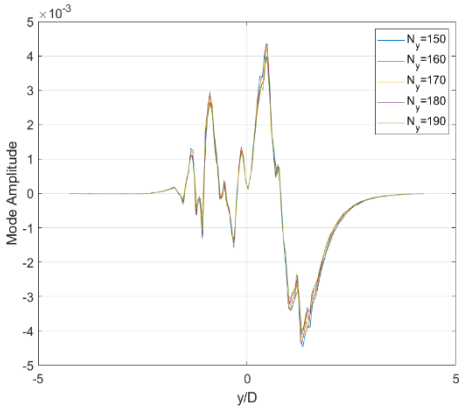

Figure 7.3 (b)

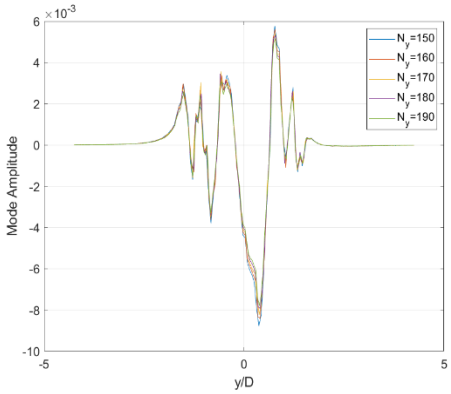

Figure 7.3 (c)

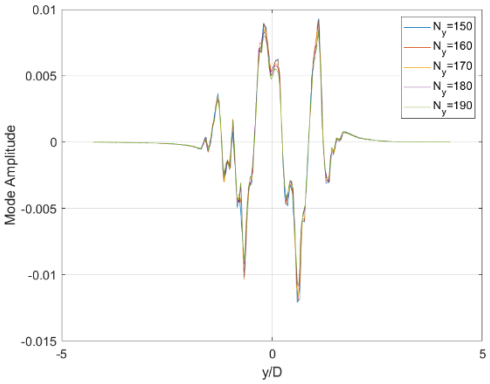

Figure 7.3 (d)

Figure 7.3 *Convergence analysis amplitude mode* 1 *at* x/D=5 *at the shedding frequency* f_{SH} *(a),* $2f_{SH}$ *(b),* $3f_{SH}$ *(c),* $4f_{SH}$ *(d)*

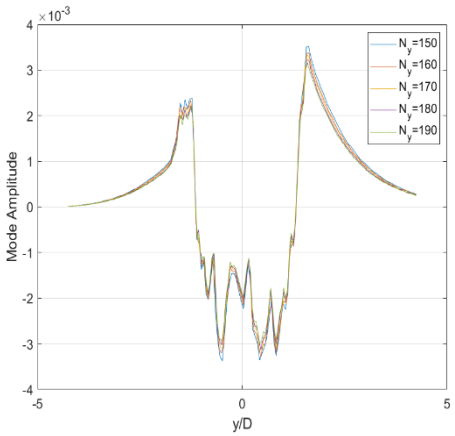

Figure 7.4 (a)

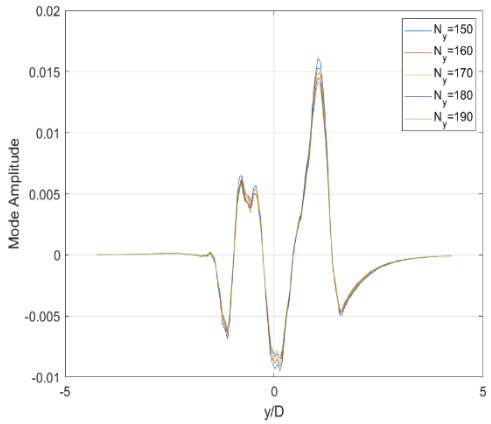

Figure 7.4 (b)

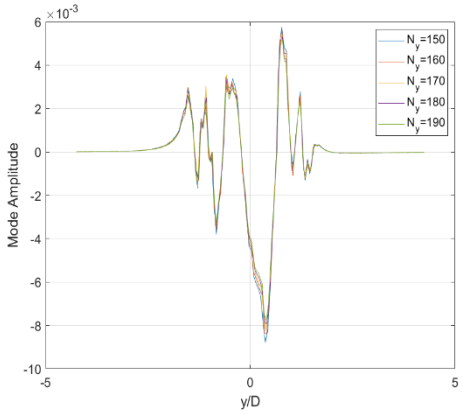

Figure 7.4 (c)

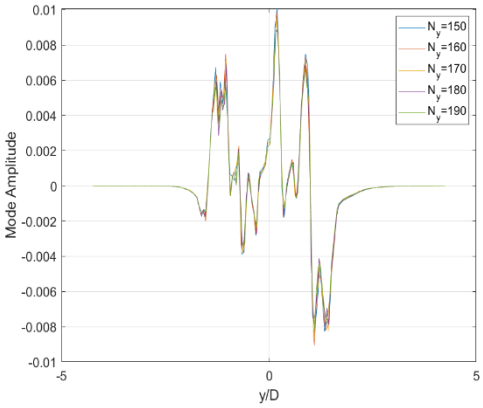

Figure 7.4 (d)

Figure 7.4 *Convergence analysis amplitude mode 2 at x/D=5 at the shedding frequency f_{SH} (a), $2f_{SH}$ (b), $3f_{SH}$ (c), $4f_{SH}$ (d)*

The convergence analysis carries satisfying results also for the crosswise direction, taking into account the first mode at the shedding frequency, between the last two curves (N_Y = 180, N_Y = 190) a discrepancy of about 3% is retrieved like in the previous analysis. As a result, in order to obtain a comparable resolution in both crosswise and streamwise direction N_Y = 190 is selected for the rest of work. The solid cylinder together with the porous medium is taken into account inside the domain assigning a zero weight to them. As a result they remain part of spatially coherent SPOD modes, but they are not considered in the SPOD computation.

7.2 SPOD results

In this section, the results of the Spectral Proper Orthogonal Decomposition (SPOD) analysis are presented considering the grid of points, whose dimensions are selected in the previous section. Initially, the SPOD energy distribution among the modes is discussed, followed by a detailed examination of the mode amplitudes based on the two velocity components and the static pressure field. Eventual presence of symmetries with respect to the centre line y/D = 0 will be discussed as well.

7.2.1 SPOD energy mode

First, SPOD eigenvalues are plotted as a function of the Strouhal number for each mode, along with the corresponding energy contribution expressed as a percentage of the total energy.

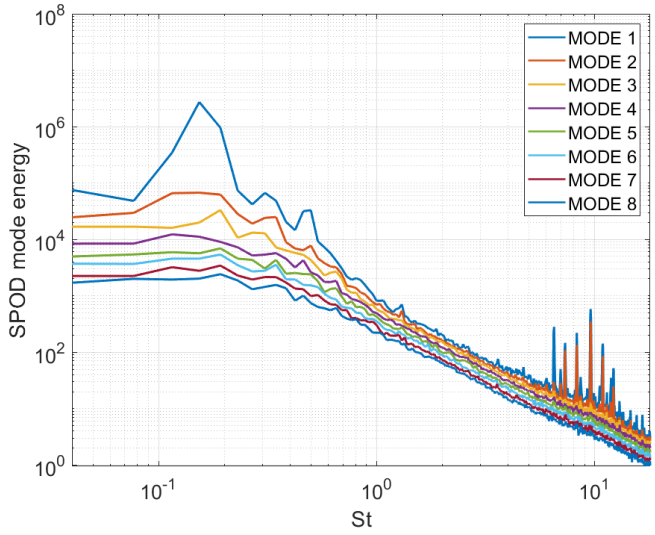

Figure 7.5 *SPOD mode energy spectrum*

From the energy spectrum (figure 7.5), it can be seen that, especially in the low frequency range, the first mode carries a relevant amount of energy compared to the other modes. The most prominent peak is observed at the fundamental shedding frequency (i.e. St = 0.154), while additional local peaks occur at both odd and even harmonics of this frequency. Finally the local peaks in the high frequency range are linked to the vortex shedding in the small cylinders of the porous medium. The dominance of the first mode

in terms of energy contribution is further confirmed by plotting the percentage of the total energy associated with each mode.

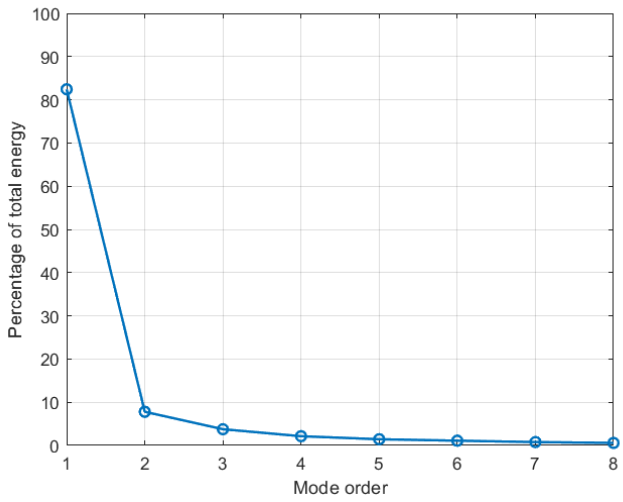

Figure 7.6 *Percentage of total energy for each mode*

Consistently, it is found that the first mode accounts for approximately 82% of the total energy, while the second mode contributes around 8%. The remaining energy is distributed among the higher-order modes. The contribution of the first mode becomes even more significant (about 96 %) when the energy percentage is computed exclusively at the shedding frequency (figure 7.7), suggesting a low-rank behaviour.

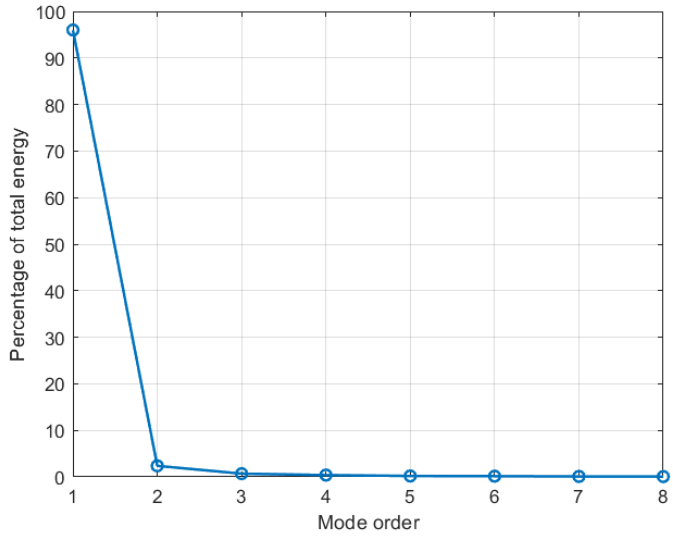

Figure 7.6 *Percentage of total energy for each mode at the shedding frequency*

7.2.2 SPOD modes based on velocity components

At this stage, the first mode amplitudes based on both velocity components are plotted at the shedding frequency, as well as at its first odd and even harmonics.

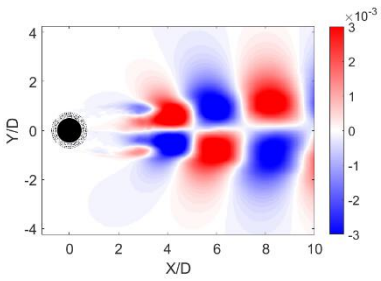

Figure 7.7 (a)

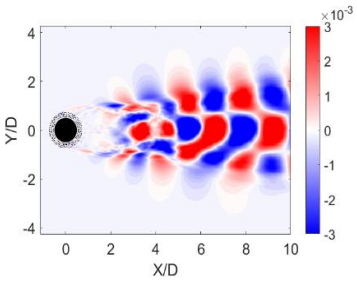

Figure 7.7 (b)

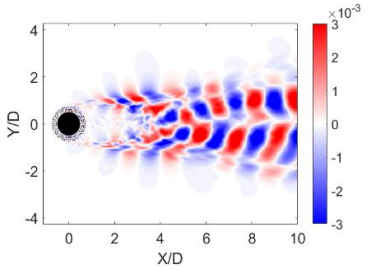

Figure 7.7 (c)

Figure 7.7 *First mode amplitude based on streamwise velocity component at the shedding frequency f_{SH} (a), $2f_{SH}$ (b) and $3f_{SH}$ (c)*

From above figures it can be seen that mode amplitudes based on streamwise velocity component at the shedding frequency f_{SH} and at $3f_{SH}$ show an antisymmetric pattern with respect to the centre line y/D = 0. The former resembles a typical form of vortex shedding and it represents the advection of such vortical structures along the downstream direction. By contrast the mode amplitude at $2f_{SH}$ has a symmetric pattern.

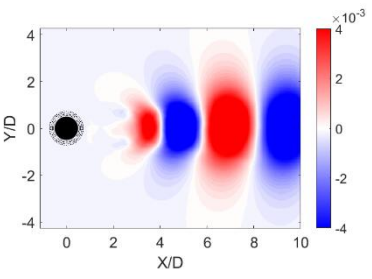

Figure 7.8 (a)

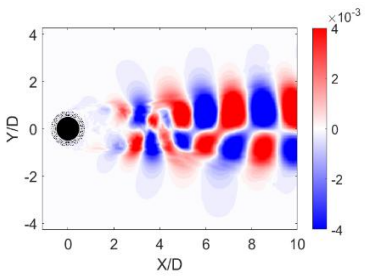

Figure 7.8 (b)

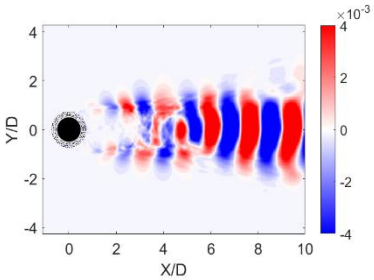

Figure 7.8 (c)

Figure 7.8 *First mode amplitude based on crosswise velocity component at the shedding frequency f_{SH} (a), $2f_{SH}$ (b) and $3f_{SH}$ (c)*

Contrary to what is been found for the streamwise mode amplitude, the mode pattern at f_{SH} and $3f_{SH}$ are symmetric with respect to the centre line, while at $2f_{SH}$ is symmetric about x-axis. However, it is evident that such symmetries are not always clearly discernible, and in some cases, they only emerge after the onset of vortex shedding. Extending the simulation time may lead to a more symmetric distribution.

7.2.3 SPOD results based on static pressure

To conclude this section, first mode based on static pressure is plotted at the same frequencies above considered.

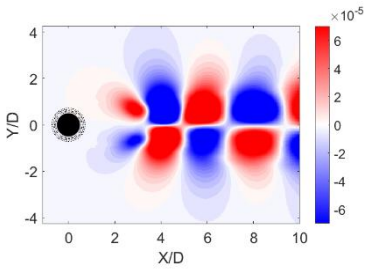

Figure 7.9 (a)

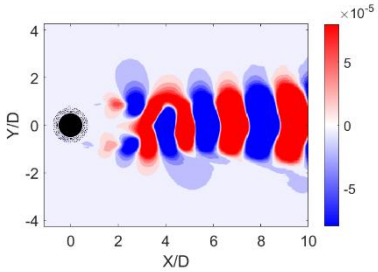

Figure 7.9 (b)

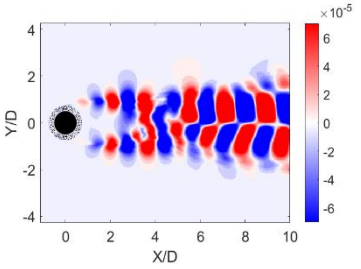

Figure 7.9 (c)

Figure 7.9 *First mode amplitude based on static pressure at the shedding frequency f_{SH} (a), $2f_{SH}$ (b) and $3f_{SH}$ (c)*

SPOD modes based on static pressure have a similar pattern to that described for those based on streamwise velocity component. The even harmonics of the shedding frequency have a symmetric pattern with respect to the centre line, while the odd harmonics are antisymmetric. However, at the same frequency, the pressure mode amplitudes are two order of magnitude smaller than those found for both velocity components.

7.3 Wavenumber spectrum

Up to this point, a basic analysis has been conducted on the energy spectrum and on the symmetries present in the spatial patterns of the SPOD modes. The next step is to post-process SPOD results in order to investigate about the eventual presence of a feedback contribution that induces pressure fluctuations on the cylinder surface at the shedding frequency. In other words, the goal is to provide a physical interpretation of what, in equivalent terms, it has been called diffraction mechanism and to support a corresponding interpretation of the porous coating's effectiveness in mitigating noise. Since in the previous section it has been underlined that the first mode carries a dominant energetic contribution at the shedding frequency, it is selected for the subsequent analysis. To enhance the potential presence of a contribution that propagates upstream, a Fourier transform along the streamwise direction is performed for the first mode based on x-velocity at the shedding frequency.

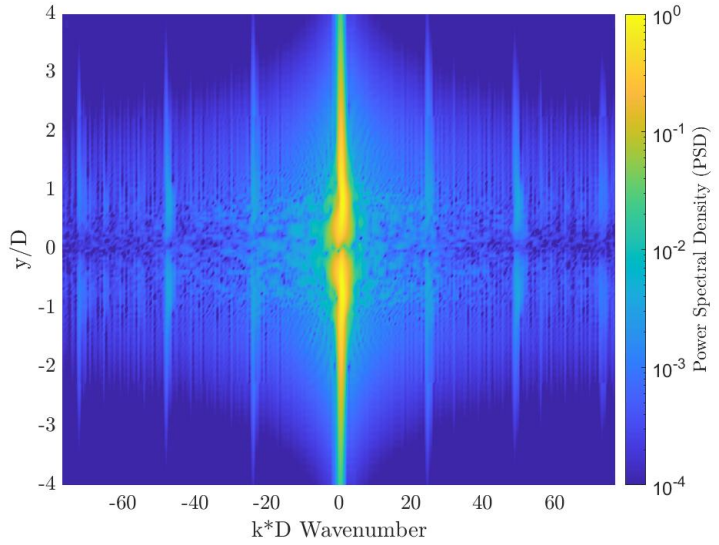

Figure 7.10 *Wavenumber spectrum along the streamwise direction of the first mode at the shedding frequency based on x-velocity as a function of wavenumber and crosswise location*

From figure 7.10, it can be noted a dominant contribution marked in yellow which is linked to the convection of large scale vortices downstream. From the plot it can be obtained the corresponding wavenumber of such contribution and, consequently, the propagation velocity:

$$V_p = \frac{\omega_{sh}}{k} = 25.81 \frac{m}{s} \cong 0.86\, U_\infty$$

(7.1)

Moreover, consistently with pattern found in the previous section, this contribution becomes zero along the x-axis. Since the objective is to investigate potential upstream influences, particular attention is needed to the range of negative wavenumbers. Within this range, three distinct local peaks can be clearly identified. To better identify these local peaks the PSD is averaged on the crosswise direction and one of the aforementioned contribution is selected for the following analysis.

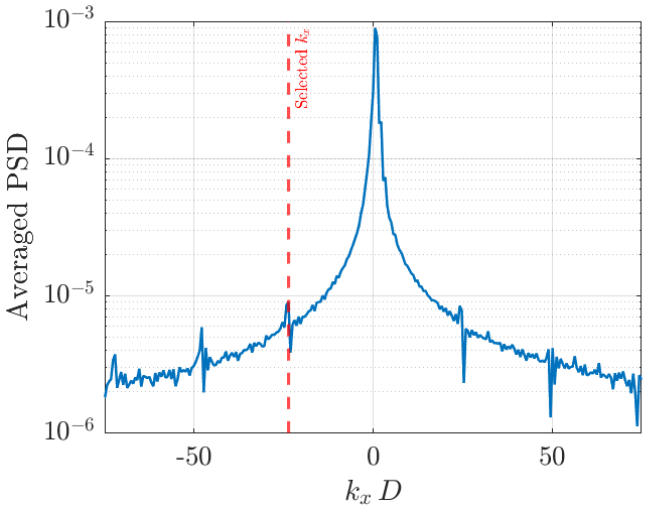

Figure 7.11 *Averaged wavenumber spectrum along the crosswise direction as a function of dimensionless wavenumber*

The three contributions within the negative wavenumber range are located at wavenumbers that are approximately twice the value of the preceding one. Moreover, each upstream-propagating component has a symmetric counterpart with respect to the main peak, which propagates downstream. At this stage, to retrieve the spatial mode the inverse Fourier transform is performed at the wavenumber selected in figure 7.11 and the result is reported in the following figure.

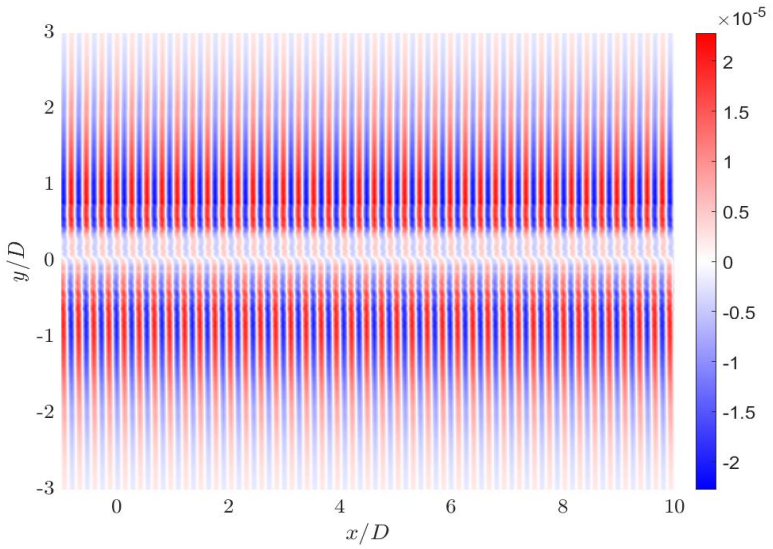

Figure 7.12 *Filtered mode at the selected wavenumber (k_xD = -23.66) based on x-velocity*

As can be observed, a feedback contribution is retrieved that remains minimal along the x-axis and appears to propagate from the wake toward the surface. However, it should be noted that the direction of this contribution cannot be directly inferred from the figure above; a time-resolved animation would be required to properly illustrate this aspect, which is not included here. The propagation velocity of this contribution can be derived from Equation 7.10, yielding a value of about 1.23 m/s. The same passages can be also repeated considering the second local peak observed in the range of negative wavenumber.

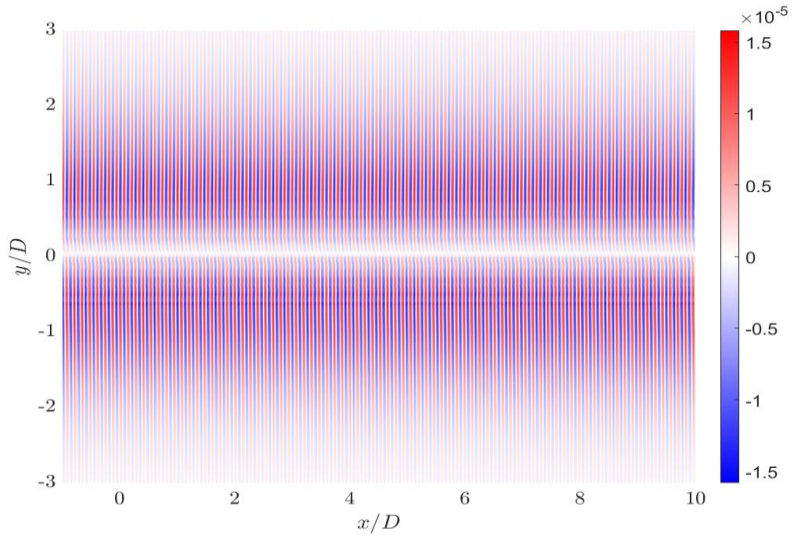

Figure 7.13 *Filtered mode at the selected wavenumber (k_xD = -47.88) based on x-velocity*

A similar pattern to that represented in the figure 7.12 is observed, with a wavelength, and a propagation velocity, which are the half of that found previously. To assess the validity of the adopted method, the wavenumber relative to the dominant peak is selected, and performing the inverse Fourier transform, a typical vortex shedding pattern should be found.

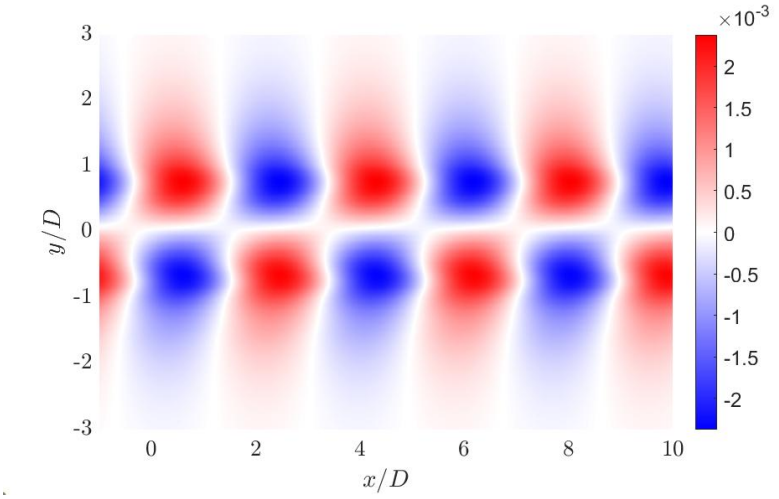

Figure 7.14 *Filtered mode at the wavenumber of the dominant peak*

As can be seen from figure 7.14, this presupposition is fully respected. Nevertheless, the precise origin of the vortex shedding cannot be identified, as only a single wavenumber has been selected rather than the full spectral content. As a consequence, the propagation appears constant. For this reason, the x-axis (x/D) could be omitted from Figures 7.12, 7.13, and 7.14. To complete the analysis, same calculations can be repeated considering the first mode at the shedding frequency based on crosswise velocity component. Performing the Fourier transform along the streamwise axis, a similar distribution to that shown in figure 7.10 is retrieved, with the exception that the pattern is symmetric with respect to the x-axis, consistently with what it has been found in the previous section (Figure 7.15).

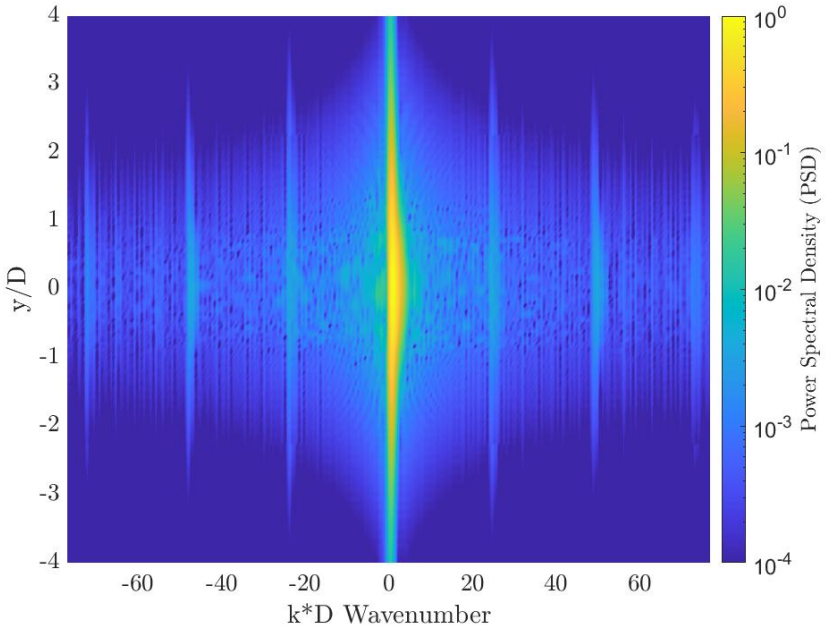

Figure 7.15 *Wavenumber spectrum along the streamwise direction of the first mode at the shedding frequency based on y-velocity as a function of dimensionless wavenumber and crosswise position*

Focusing on the negative wavenumber spectrum same peaks at the same dimensionless wavenumber to the those found for the streamwise component are retrieved. Following the same approach the first contribution is selected and the inverse Fourier transform is performed to retrieve the filtered mode in the spatial domain.

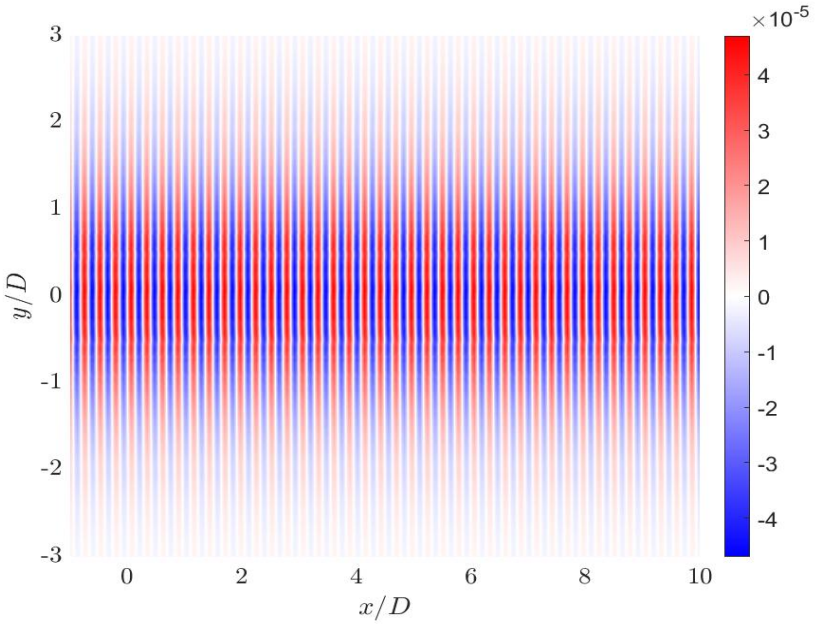

Figure 7.16 *Filtered mode at the selected wavenumber (k_xD = -23.66) based on y-velocity*

A feedback contribution that, contrary to that found for the streamwise velocity, has its maximum amplitude along the centre line y/D = 0 is got. The existence of this feedback contribution that propagates from the wake to the surface suggests that the acoustic energy comes from the flow itself, as hypothesized in the first chapter. Consequently the present problem needs to be formulate as a diffraction problem of flow sources on the surface. Za2Some conclusions and hypotheses about the origin of these contributions, their role in imposing pressure fluctuations at the shedding frequency on the cylinder surface, their dependence on the vortex formation length will be drawn in the final chapter.

7.4 Spectral coherence

Carrying on with the post-processing of SPOD results, spectral coherence between the pressure mode on the cylinder surface and velocity modes in the wake has been computed. Mode 1 at the shedding frequency is always included in the analysis. Spectral coherence is computed as follows:

$$\gamma_{p,u} = \frac{mode_{u,v}\, mode_p^*}{|mode_{u,v}||mode_p|} \tag{7.2}$$

Where the * represents the complex conjugate of the pressure mode, which is been evaluated on the bare cylinder surface in both leeward and windward regions. Results for the latter region are reported in the following figures.

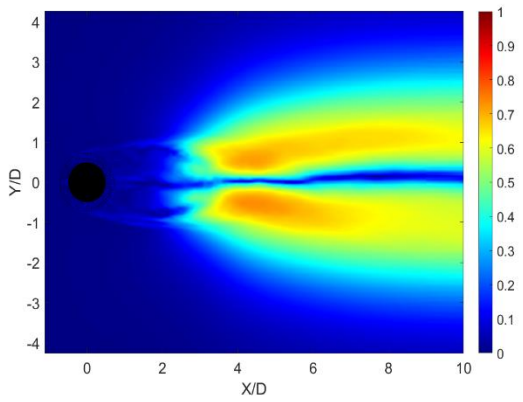

Figure 7.17 (a)

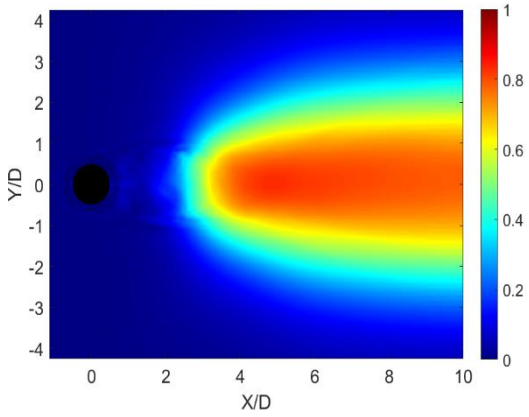

Figure 7.17 (b)

Figure 7.17 *Magnitude of the spectral coherence at the shedding frequency between streamwise velocity mode (a) crosswise velocity mode (b) in the wake and pressure mode at θ=40° (leeward region)*

Consistently with the feedback contributions found in the previous section peak values of spectral coherence are observed away from the centre line for the streamwise velocity and near the centre line, more precisely near the onset of vortex shedding, for the crosswise velocity mode. A further result, which aligns with the findings presented in the previous section, indicates that crosswise components are more prone to generating pressure fluctuations on the surface. This tendency is also reflected in the amplitudes of the feedback contributions, as illustrated in Figures 7.12 and 7.17. Same results are now reported for the windward region. Similar patterns are retrieved also for this region, however it can be clearly seen that the values are lower than those observed in the leeward region, this further highlights the fact that these feedback contributions diminish with increasing distance.

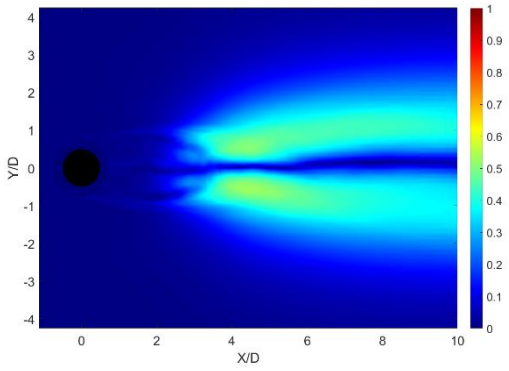

Figure 7.18 (a)

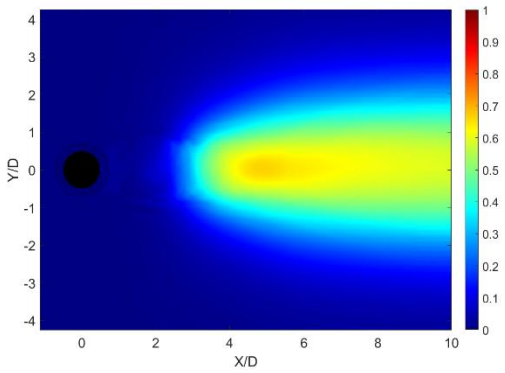

Figure 7.18 (b)

Figure 7.18 *Magnitude of the spectral coherence at the shedding frequency between streamwise velocity mode (a) crosswise velocity mode (b) in the wake and pressure mode at θ=130° (windward region)*

To further support this analysis, the evaluation is extended by computing the spectral coherence between the velocity mode at a single point within the wake and the pressure mode distributed along the bare cylinder surface, in accordance with Equation 7.2.

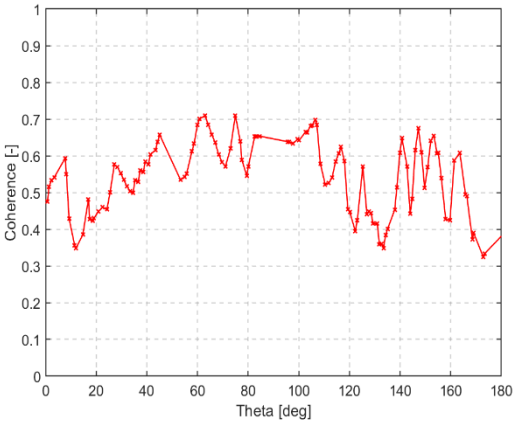

Figure 7.19 (a)

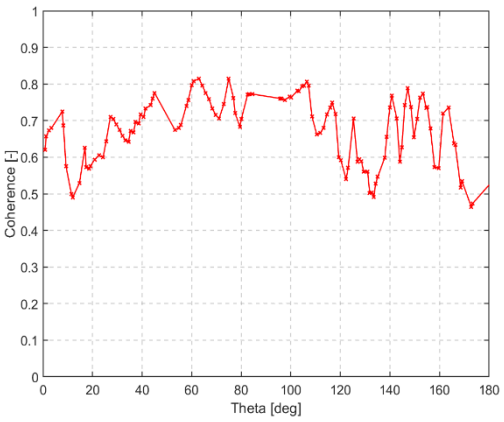

Figure 7.19 (b)

Figure 7.19 *Magnitude of spectral coherence at the shedding frequency between streamwise velocity mode (a), crosswise velocity mode (b) at (4D, 0.5*D, 0) and pressure mode around the bare cylinder*

The above figures report the spectral coherence values as a function of angular coordinate around the bare cylinder. As can be observed, the previously highlighted findings are not clearly identifiable here, due to an irregular trend characterized by sudden drops in coherence values. This is likely due to the fact that an eventual feedback contribution,

before reaching the solid cylinder, has to pass through the porous medium. Consequently, it is notably weakened leading to the decrease of the coherence values. To validate this hypothesis, the pressure mode needs to be evaluated around the outermost layer, therefore no porous layers are encountered by the feedback contribution during its path and a smoother distribution could be obtained.

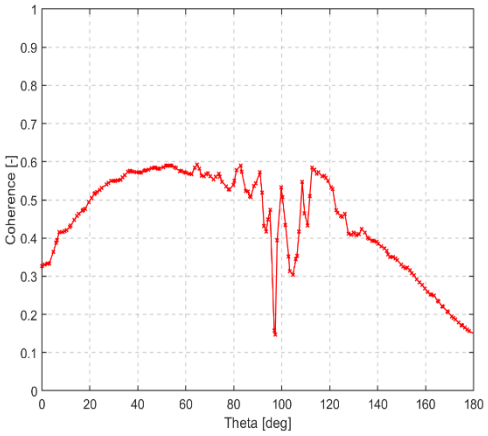

Figure 7.20 (a)

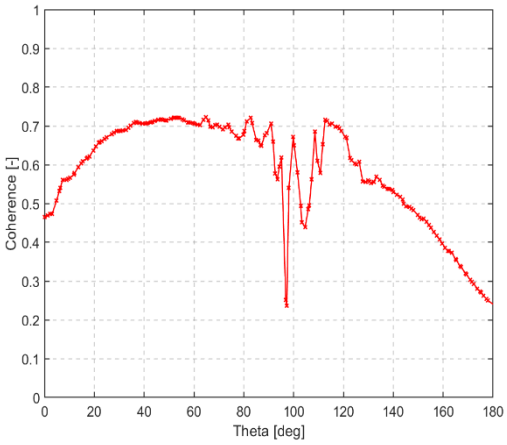

Figure 7.20 (b)

Figure 7.20 *Magnitude of spectral coherence at the shedding frequency between streamwise velocity mode (a), crosswise velocity mode (b) at (4D, 0.5*D, 0) and pressure mode around the outermost layer*

The deductive reasoning outlined above is supported by the results shown in Figure 7.20, as a clearer distribution is observed with the exception of the separation region, where sudden drops of coherence values are found. However it is again confirmed that moving from leeward ($0 < \theta < 90°$) to the windward region ($90° < \theta < 180°$) the feedback contribution is notably weakened, leading to lower spectral coherence values.

Chapter 8: Conclusions

The present work elucidates the physical connection between the effects on near-wake development and relative noise mitigation performance of the structured porous coating. For this purpose results coming from an high-fidelity simulation based on LBM methods has been post-processed. Far-field data analysis reveal that, in the low-frequency regime, the dominant noise is generated by quadrupolar sources located in the wake and linked to unsteady velocity fluctuations, while in the high-frequency range a different noise generation mechanism is observed and it is linked to the surface roughness of the porous coating. However, the previous statement disagrees with the most common view provided by Curle's analogy, which states that, at low Mach numbers, the quadrupolar source can be considered negligible with respect to the dipolar source, which is linked to the pressure fluctuations acting on the cylinder surface. This findings, together with results obtained by Zamponi et at. (2024), suggest that the present problem should be formulated as a diffraction problem of the flow sources (i.e. quadrupole), while the dipolar field is the result of scattering on the cylinder surface of acoustic waves of the quadrupolar source in the wake. Nevertheless an overall quasi-dipolar pattern is retrieved in the far-field, since the scattered field is characterized by a dipolar directivity. The relevance of the flow source is also confirmed through a coherence analysis between far-field pressure, near-field pressure and velocity fluctuations. Indeed it has been found that the latter has the greatest impact on the far-field noise, showing greater coherence values at the shedding frequency than those observed evaluating the coherence between near-field and far-field pressure at the same frequency. To provide a physical interpretation of these results, effects of the porous coating on the near-wake development have been analysed. From velocity contours, it can be seen that as the flow penetrates the porous medium it dissipates part of its energy and a low-energy region is formed downstream the cylinder. As a result, the shear layers are more relaxed and the onset of vortex shedding is shifted downstream, increasing what it is normally referred to as vortex formation length. This parameter has a relevant impact on aeroacoustic results, since it reduces the efficiency of scattering mechanisms reducing the relevance of the dipolar source on the far-field noise. However, it must be kept in mind that noise mitigation performance depend also on the porous medium properties, since it is able to impact on the increasing of vortex-formation length and, consequently, on the relative weight of the acoustic sources. The second main

result of the present work is to have elucidated a physical interpretation of what, in equivalent terms, it has been called diffraction mechanism exploring the potential presence of a feedback mechanism which induces pressure fluctuations on the cylinder surface at the shedding frequency. For this reason, Spectral Proper Orthogonal Decomposition based on Welch's method have been performed. It has been found that, at the shedding frequency, the first mode carries the most relevant amount of energy and it is selected for the subsequent analysis. For this mode Fourier transform along the streamwise direction have been performed and a feedback contribution in the negative wavenumber range has been retrieved. This contribution is deemed to be responsible for inducing pressure fluctuations. Hence, thanks to the increasing of the vortex formation length, this contribution should travel for a longer distance and it tends to be weakened, and induced pressure fluctuations are weakened as well, elucidating a physical link between increasing of the vortex formation length and loss of efficiency of the scattering mechanism. However the precise mechanism through which such feedback contribution is generated is not clear, only limited hypotheses can be formulated, such as velocity fluctuations induced by large-scale vortices through Biot–Savart induction. To better understand the precise mechanism a stability analysis is required and this represents a direction for future investigations. As can be observed, the present work has been conducted without performing a direct comparison between the porous and baseline configurations, as it is based on a single simulation. Drawing comparisons with other studies could lead to misleading conclusions, given that different parameters - such as flow velocity and geometry - may have been employed. For this reason, no direct comparisons have been included in this study. Furthermore, it should be emphasized that results here presented have been obtained with partial results, a longer simulation time to achieve the full convergence could potentially lead to more accurate and reliable outcomes. The present data set could be also used to directly integrate the different components of Lighthill's tensor through the use of the commercial software Optydb, obtaining the noise source contributions to the far-field acoustic pressure (or power) according different frequency bands. This will be a topic for a future work as well. Finally the present work makes light for design of different flow control and related noise mitigation strategies, indeed the downstream shifting of outbreak of vortex shedding instability represents a valid criterion for achieving acceptable noise mitigation

performance. The presence of the porous coating is not essential for producing the same effect and new technologies could be explored.

Bibliography

C. Xia, Z. W. (2018). POD analysis of the wake behind a circular cylinder coated with porous media. *J. Vis.*

E.J.G. Arcondoulis, Y. L. (2019). Structured porous material design for passive flow and noise control of cylinders in uniform flow. *Materials 12*.

E.J.G. Arcondoulis, Y. L.-C. (2023). Internal shear layer and vortex shedding development of a structured porous coated cylinder using tomographic particle image velocimetry,. *J. Fluid Mech.*

E.Sarradj, T. (2016). Circular cylinders with soft porous cover for flow noise reduction. *Exp. Fluids*.

Geyer, T. (2020). Experimental evaluation of cylinder vortex shedding noise reduction using porous materia. *Exp. Fluids*.

H. Liu, J. W. (2012). Prediction of aerodynamic noise reduction by using open-cell metal foam. *J. Sound Vib.*

H. Naito, K. F. (2012). Numerical simulation of flow around a circular cylinder having porous surface. *Phys. Fluids* .

Herrmann, D. (2007/2008). *A Study of the Suitability of PowerFLOW as an Educational Engineering Design Tool for Undergraduate Students.*

J. Aguiar, H. Y. (2016). Passive flow/noise control of a cylinder using metal foam. *the 23rd International Congress on Sound and Vibration, The International Institute of Acoustics and Vibration*.

Kaibin Wena, E. J. (2021). Structure resolved simulations of flow around porous coated cylinders based on a simplified pore-scale model. *Aerospace Science and Technology*.

Lighthill, J. M. (1951). *On the sound generated aerodynamically* .

Liu, R. M. (2024). Cylinder flow and noise control by active base. *Journal of Fluid Mechanic* .

Oliver T. Schmidt, T. C. (2020). Guide to Spectral Proper Orthogonal Decomposition. *AIAA Journal* .

P.E. Doak. (1960). Acoustic radiation from a turbulent fluid containing foreign bodies. *Proc. Roy. Soc. Lond. A Mat.* .

R. Zamponi, F. D. (2024). Relevance of quadrupolar sound diffraction on flow-induced noise from porous-coated cylinders. *Journal of Sound and Vibration* .

R. Zamponi, S. S. (2023). Effect of porosity on Curle's dipolar sources on an aerofoil in turbulent flow. *J. Sound Vib.*

Rego, L., Avallone, F., Ragni, D., & Damiano, C. (2020). Jet-installation noise and near-field characteristics of jet surface interaction. *Journal of Fluid Mechanic* .

S. Sadeghipour, S. S. (2020). Control of flows around bluff bodies mediated by porous materials. *Exp. Therm. Fluid Sci.* .

S. Sharma, T. G. (2023). On the influence of porous coating thickness and permeability on passive flow and noise control of cylinders . *J. Sound. Vib.*

S.A. Showkat Ali, X. L. (2016). Bluff body flow and noise control using porous media. *22nd AIAA/CEAS Aeroacoustics Conference, American Institute of Aeronautics and Astronautics, Lyon, France*.

T. Sueki, T. T. (2010). Application of porous material to reduce aerodynamic sound from bluff bodies. *Fluid Dyn. Res. 42*.

X. Gloerfelt, F. P. (2005). Flow-induced cylinder noise formulated as a diffraction problem for low Mach numbers. *J. Sound Vib. 287* .

Y. Sato, Y. H. (2021). Mechanism of reduction of aeroacoustic sound by porous material: Comparative study of microscopic and macroscopic models. *J. Fluid Mech.*

Simulia PowerACOUSTICS 2024 User’s Guide

Simulia PowerFLOW 2024 User’s Guide

Simulia PowerFLOW 2024 PowerCASE USER'S GUIDE

Aeroacoustic – Course slides – Aerodymanic noise